Mechanical Systems and Signal Processing 127 (2019) 441–462

Contents lists available at ScienceDirect

Mechanical Systems and Signal Processing

journal homepage: www.elsevier.com/locate/ymssp

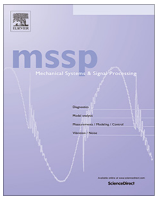

# A load-dependent PWA-$H_\infty$ controller for semi-active suspensions to exploit the performance of MR dampers

Jian Wu [a], Hongliang Zhou [a], Zhiyuan Liu [a,*], Mingqin Gu [b]

[a] *Department of Control Science and Engineering, Harbin Institute of Technology, Harbin 150080, China*
[b] *Alibaba AI Lab, Hangzhou 310000, China*

ARTICLE INFO

*Article history:*
Received 2 November 2018
Received in revised form 19 January 2019
Accepted 13 March 2019
Available online 21 March 2019

*Keywords:*
Semi-active suspension
MR damper
$H_\infty$ control
Piecewise affine control law
Time-varying load

ABSTRACT

Magnetorheological (MR) dampers enable wide-range adjustment of damping and are considered as promising actuators for suspension performance optimization. However, MR dampers also exhibit complex nonlinearities, including hysteresis and bi-viscosity. Moreover, in addition to handling road irregularities, the suspension system needs to adjust its performance according to variations in vehicle load. The above nonlinearities and requirements both bring challenges to the design of semi-active suspension controllers. In this paper, the nonlinearities of MR dampers are handled with a piecewise modeling method, and the vibration attenuation is realized by designing a static piecewise-affine (PWA) $H_\infty$ controller. Furthermore, to deal with the time-varying load and to fully utilize the capability of MR dampers, a parameter-dependent piecewise-quadratic Lyapunov function (PDPQLF) is employed, which results in a load-dependent PWA (LDPWA) $H_\infty$ controller. Simulation and experimental results under random, bumpy and sinusoidal excitations show that the proposed controller can achieve enhancements on both comfort and handling performance. Above all, the proposed method enables effective high-frequency vibration suppression for underload conditions, while for overload conditions, the low-frequency performance is more significantly improved.

© 2019 Elsevier Ltd. All rights reserved.

## 1. Introduction

As key components of vehicles, suspension systems have been studied for many years, and numerous methods related to structures [1], actuators [2] and control [3] have been proposed to improve suspension performance. When faced with road surface irregularities, vehicle suspensions are required to (1) enhance the comfort performance, (2) ensure the handling performance, and (3) limit the suspension deflection. These requirements, however, are conflicting to each other and a tradeoff has to be involved [4]. More complicated, the requirements of suspensions will change with the variation of vehicle loads [5]. For example, a vehicle which is configured for heavy load should have a relatively stiff suspension. However, when the load is removed, the suspension will be excessively stiff or over-damped, which results in deteriorative comfort performance. Conversely, when the suspension is configured for an unloaded condition, it will be too soft to support additional weight. Therefore, it is imperative to design a suspension system which can achieve the multi-objective performance for both road excitations and load variations. Since traditional passive suspensions cannot be adjusted online, semi-active and active suspensions have attracted more and more attention of industries and academia to deal with the above problems.

---

[*] Corresponding author.
*E-mail addresses:* vijaychn217@gmail.com (J. Wu), zhouhongliang@hit.edu.cn (H. Zhou), liuzy_hit@hit.edu.cn (Z. Liu), mingqin.gmq@alibaba-inc.com (M. Gu).

https://doi.org/10.1016/j.ymssp.2019.03.018
0888-3270/© 2019 Elsevier Ltd. All rights reserved.

Active suspensions, which can inject energy to suspension systems by adjusting the active force directly, have powerful adjustment capabilities and can effectively handle the complex road and load conditions [6–8]. Besides many literatures on the attenuation of road disturbances, the researches of active suspension on load adaptation can be traced back to the 1990s. For example, by combining an air spring and an air responsive shock absorber (stiff for a high air pressure which is caused by a heavy load and soft for a low air pressure which corresponds to a light load), an active suspension which can respond to both road and load conditions is designed and patented by the Monroe corp. [9]. Further, as a modification of this concept, a booster which enables the pressure communication between the air spring and the shock absorber is proposed by the Tenneco Inc. [10]. In addition to these suspension structure innovations, some researchers also achieve the load adaption property by designing control algorithms of the active force. For example, a load-dependent controller is creatively given in [11] where the gain matrix can vary according to the vehicle load to achieve a better multi-objective performance. This parameter-dependent control strategy is further expanded in [12] to design the vehicle active suspension controllers which consider both the vehicle inertial parameter variations and the time delays of electro–hydraulic actuators. Recently, an adaptive controller for active seat suspensions has been proposed in [13] and the controller is experimentally verified to show good performance on vibration control and high system robustness to the operator's mass variations. Above all, the load-adaptive (or load-dependent) active suspensions have been heavily studied in the past two decades. However, the high structure complexity and the huge power consumption will inevitably increase the cost and limit the application of active suspensions.

Conversely, semi-active suspensions, which can only dissipate energy from the vibration system by adjusting the damping force of shock absorbers, have a compact size and require very little energy supply [14–16]. Although semi-active suspensions are not as adjustable as active suspensions, they are more convenient for practical applications. For the above reasons, the development of load-adaptive semi-active suspensions has attracted the interest of industry. For example, in [17], an integrated damper which includes a damper and a valve block is designed. The valve block has a spring pilot which can indicate the pressure on the spring. This patented damper enables damping response to load conditions without relying on conventional air (or hydraulic) springs. However, the assembly and manufacture of this damper are not a short-term job. Therefore, design of a load-adaptive algorithm for semi-active suspensions has become a research trend. Currently, magnetorhelogical (MR) dampers which are treated as promising semi-active actuators due to their wide adjustment range and fast response speed are drawing more and more attention [18,19]. Moreover, this actuator can be easily driven by a current of 0 A–3 A, which is convenient to be integrated into traditional vehicle electrical systems. However, MR dampers also show up complex nonlinearities including dissipative constraint, bi-viscous and hysteresis [20–22], and the existing load-adaptive controllers for active suspensions cannot be directly transplanted into the MR semi-active suspensions. Thus, these nonlinearities pose challenges to the controller design. As a pioneer, a load-dependent LPV/$H_2$ controller is designed for the MR semi-active suspensions in [23], where the time-varying load is treated as a scheduling parameter and the actuator nonlinearities are handled by an inverse MR model. The design approaches based on inverse MR models always involve a two-step technique. In the first step, a damping force controller is designed based on a linear suspension model, and in the second step, an inverse model which reflects the dynamics of MR dampers is used to transform the damping force to the driving current. However, as illustrated in [24,25], this method may lead to unpredictable results and ensure neither the system stability nor the suspension performance, since the capabilities of MR dampers or the constraints on damping force have not been concerned in the first step. For this reason, in [26], the authors of this paper have proposed a piecewise MR suspension model to handle the actuator nonlinearities, where the nonlinear force constraint is approximated with constant constraints of subsystems. Then, a piecewise affine $H_\infty$ (PWA-$H_\infty$) controller is designed by using a global quadratic Lyapunov function (GQLF). The method is concise and is convenient to be applied online. However, the employment of GQLF may produce conservative results, since a unique Lyapunov function is used for all the piecewise subsystems. Another problem is that the proposed PWA-$H_\infty$ controller cannot adapt to the load variation.

In this paper, a parameter-dependent piecewise quadratic Lyapunov function (PDPQLF) is employed to design a load-dependent PWA-$H_\infty$ (LDPWA-$H_\infty$) controller. Considering the capability of MR dampers, a piecewise constrained MR suspension model is firstly introduced to design the damping force controller. An inverse MR damper model is then utilized to generate the driving current. To handle the road irregularities, the force tracking error of the inverse model and the load variation, a load-adaptive robust controller is further designed by using a PDPQLF. Finally, the proposed strategy of this paper is verified by simulations and experiments under different external excitations. The main contributions in this paper are summarized as follows.

- Through the piecewise modeling of MR semi-active suspensions, the difficulty of concerning the realizability of damping force in the classic inverse model based control design can be solved. Additionally, compared with other models with nonlinear constraints [27,28], the proposed model is more convenient for the off-line design and the on-line application of suspension controllers.
- With the employment of PDPQLF which empowers the controller a load-adaptive ability, the damping force in each subsystem can act up to its own constraint condition to realize the optimal suspension performance. Compared with traditional $H_\infty$ methods which consider the unconstrained cases [29] or possess a high-order dynamic feedback controller [30], the proposed method can guarantee the nonlinear damping force constraint with a simple static feedback controller. Additionally, the proposed method can utilize the capabilities of MR dampers more comprehensively than the method in [26].

- The effectiveness and applicability of the proposed controller in this paper are verified through a hardware implementation in accord with actual vehicle electronic systems and bench tests under sinusoidal excitations.

The remainder of this paper is organized as follows. Section 2 will introduce the piecewise model of semi-active suspensions and the control problem. Furthermore, in Section 3, a detailed design process of the LDPWA-$H_\infty$ controller will be given. Simulation and experimental results will be discussed in Sections 4 and 5, respectively.

## 2. Problem statement

### 2.1. Piecewise model of semi-active suspensions

The vertical vehicle dynamics, especially the two dominant modes, sprung mass bouncing and wheel hopping, can be represented by the quarter of vehicle (QoV) model shown in Fig. 1(a), where $m_s$ is the sprung mass which represents the vehicle chassis; $m_u$ is the unsprung mass which represents the integrated mass of wheel hub, tire, MR damper, spring and linkages; $k_s$ is the spring stiffness; $c_s$ is the damping of an additional passive damper; $F$ is the damping force output by the MR damper; $k_t$ stands for compressibility of the pneumatic tire; $z_s$ and $z_u$ is the vertical displacements of sprung and unsprung masses, respectively; and $z_r$ is the excitation when a vehicle runs on uneven road. Based on the above definitions, dynamics of MR semi-active suspensions can be described as follows:

$$\begin{cases} m_s\ddot{z}_s = -k_s(z_s - z_u) - c_s(\dot{z}_s - \dot{z}_u) - F \\ m_u\ddot{z}_u = k_s(z_s - z_u) + c_s(\dot{z}_s - \dot{z}_u) - k_t(z_u - z_r) + F. \end{cases} \tag{1}$$

As illustrated in [9], load conditions can be divided into two types: static load and dynamics load. Static load is associated with the passengers of the automobile, the cargo in the automobile, and so forth. In contrast, dynamic load involves variations related to road conditions and vehicle maneuvers. Similar to the researches in [11,12,23], this paper only considers the static load variation, which makes $m_s$ in (1) a time-varying parameter. Further, as many methods have been developed to estimate the vehicle load [31,32], it is supposed that $m_s$ can be measured online and resides in an interval, thus:

$$m_1 \leqslant m_s \leqslant m_2. \tag{2}$$

To describe the dynamics on $F$, the velocity/force (V/F) character of MR dampers is given in Fig. 1(b) where $z_{\rm def} = z_s - z_u$, and the bi-viscosity and hysteresis are displayed. These complicate nonlinearities will inevitably increase the difficulty of suspension controller design. Therefore, an inverse MR model based control schema shown in Fig. 2(a) is always adopted in industrial applications and literatures. Accordingly, a damping force controller will give desired damping force, and the inverse model will change the force into the drive current of MR dampers. However, if the desired force is beyond the capability of MR dampers, the design performance will be unrealizable. For this reason, a piecewise constrained suspension model is established in [26] to describe the force boundary. Specifically, due to the bi-viscosity, MR dampers show different properties at different deflection velocity levels, thus the whole force available scope can be divided into three regions, namely the pre-yield region and the post-yield regions shown in Fig. 1(b). In Fig. 2(b), the three yield regions are further divided into $m_{\rm pst1}, m_{\rm pst2}$ and $m_{\rm pre}$ strip-type partitions with velocity bounds $p_{Li}$ and $p_{Ui}$, and the force boundaries can be approximated by constant values $q_{Li}$ and $q_{Ui}$, where $i \in \zeta$ is the index of subsystems, $\zeta := \{1, \ldots, N\}$ and $N = m_{\rm pst1} + m_{\rm pst2} + m_{\rm pre}$ denotes the whole partition number. More details about the division and approximation can be referred in [26]. Accordingly, the available region of $F$ can be declared by the following piecewise constraints:

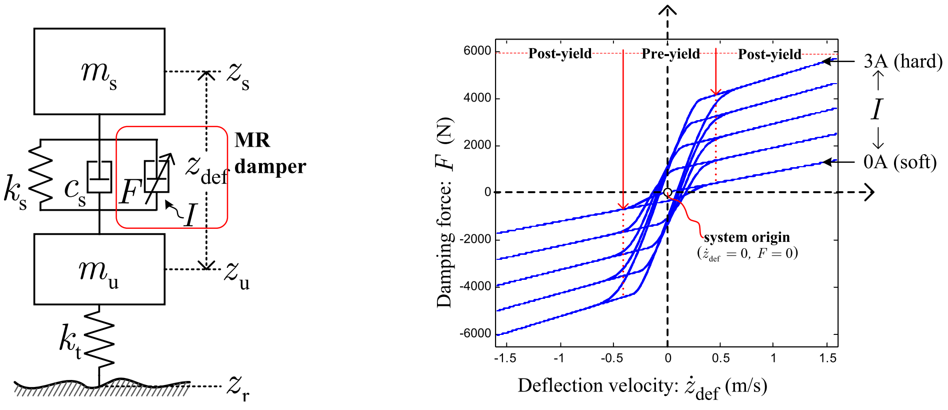

(a) (b)

**Fig. 1.** (a) MR semi-active suspension model; (b) Nonlinear actuator character.

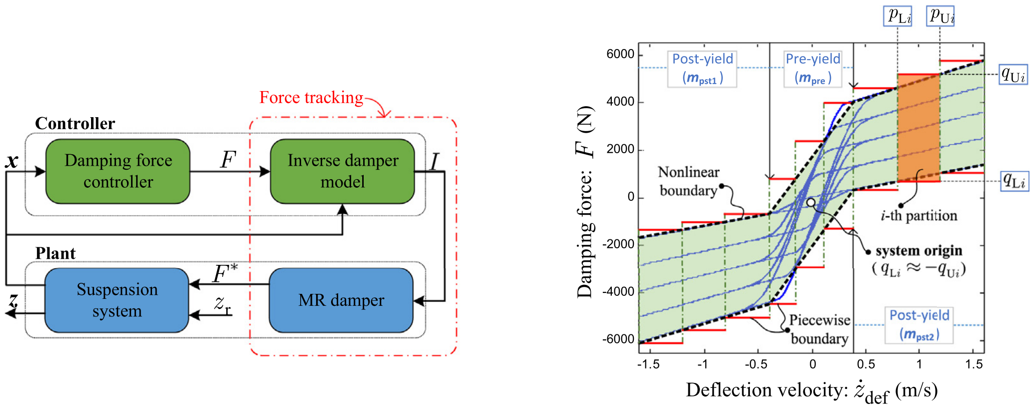

(a)

(b)

**Fig. 2.** (a) Inverse MR model based suspension control system; (b) Piecewise approximation of damping force boundary.

$$q_{Li} \leqslant F \leqslant q_{Ui}, \quad \text{if} \quad \dot{z}_{def} \in [p_{Li}, p_{Ui}], \; i \in \zeta. \tag{3}$$

**Remark 1.** The velocity intervals of partitions corresponding to post-yield and pre-yield regions are suggested to choose discriminatively. Specifically, for the pre-yield region with a stiff damping property, a smaller interval (or a bigger $m_{pre}$) should be chosen to achieve a higher approximation precision. While for the post-yield regions with soft damping properties, bigger intervals are preferred to decrease the complexity of the piecewise model.

Based on the above approximation, a piecewise constrained model of semi-active suspensions is derived. We define $\mathbf{x} = [x_1 \quad x_2 \quad x_3 \quad x_4]^T$ as the system state where $x_1 = z_s - z_u, x_2 = z_u - z_r, x_3 = \dot{z}_s$, and $x_4 = \dot{z}_u$. Then, define $\mathbf{z} = [z_1 \quad z_2 \quad z_3]^T$ as the performance output, where $z_1 = \rho_1 \ddot{z}_s, z_2 = \rho_2(z_s - z_u), z_3 = \rho_3(z_u - z_r)$, and $\rho_1, \rho_2$ and $\rho_3$ are weighting coefficients. Furthermore, by defining $u = F$ as the control input and $w = \dot{z}_r$ as the disturbance input, a state space model can be organized as follows:

$$\begin{aligned} &\dot{\mathbf{x}}(t) = \mathbf{A}_i(m_s)\mathbf{x}(t) + \mathbf{B}_i(m_s)u(t) + \mathbf{W}_i w(t), \\ &\mathbf{z}(t) = \mathbf{C}_i(m_s)\mathbf{x}(t) + \mathbf{D}_i(m_s)u(t), \quad q_{Li} \leqslant u(t) \leqslant q_{Ui}, \; \mathbf{x}(t) \in \mathcal{R}_i, \; i \in \zeta \end{aligned} \tag{4}$$

where $\mathcal{R}_i := \{\mathbf{x} | x_3 - x_4 \in [p_{Li}, p_{Ui}]\}$ denotes the definition region of the $i$-th subsystem. According to (1), the matrices in (4) can be obtained as follows:

$$\mathbf{A}_i(m_s) = \begin{bmatrix} 0 & 0 & 1 & -1 \\ 0 & 0 & 0 & 1 \\ -\frac{k_s}{m_s} & 0 & -\frac{c_s}{m_s} & \frac{c_s}{m_s} \\ \frac{k_s}{m_u} & -\frac{k_t}{m_u} & \frac{c_s}{m_u} & -\frac{c_s}{m_u} \end{bmatrix}, \quad \mathbf{B}_i(m_s) = \begin{bmatrix} 0 \\ 0 \\ -\frac{1}{m_s} \\ \frac{1}{m_u} \end{bmatrix}, \quad \mathbf{C}_i(m_s) = \begin{bmatrix} -\frac{\rho_1 k_s}{m_s} & 0 & -\frac{\rho_1 c_s}{m_s} & \frac{\rho_1 c_s}{m_s} \\ \rho_2 & 0 & 0 & 0 \\ 0 & \rho_3 & 0 & 0 \end{bmatrix},$$

$$\mathbf{D}_i(m_s) = \begin{bmatrix} -\frac{\rho_1}{m_s} & 0 & 0 \end{bmatrix}^T, \quad \mathbf{W}_i = [0 \quad -1 \quad 0 \quad 0]^T.$$

**Remark 2.** As the piecewise approximation influences only the control constraint, the system matrices $(\mathbf{A}_i(m_s), \mathbf{B}_i(m_s), \mathbf{W}_i, \mathbf{C}_i(m_s)$ and $\mathbf{D}_i(m_s))$ of different subsystems remain unchanged.

**Remark 3.** In model (4), the disturbance input is completely unknown. Thus, besides the road excitation, $w$ can also represent the approximation error of the force boundary and the force tracking error. Additionally, as the force tracking is generally realized through an open-loop schema (other implementations which rely on force feedback can also be referred in [33,34]), the inverse model accuracy will seriously influence the realization of control performance. Since the development of MR damper model or its inverse model is still a research frontier [35], designing a damping force controller that is robust to $w$ is of practical significance.

**Remark 4.** We define $\mathbf{x}(0) = 0$ when $u = 0$ as the system origin which is definitely the point where $\dot{z}_{\mathrm{def}} = 0$ and $F = 0$ in Figs. 1(b) and 2(b). Therefore, the system partitions can be divided into two classes, thus $\zeta = \zeta_0 \cup \zeta_1$, where $\zeta_0$ denotes the index set which contains the origin-included partition and $\zeta_1$ is the index set of origin-excluded partitions. According to Fig. 2(b), as the damping properties in the first and third quadrants of the V/F coordinate system are generally symmetrical, we can specify that $q_{\mathrm{L}i} = -q_{\mathrm{U}i}$ for $i \in \zeta_0$ with an acceptable approximation error.

### 2.2. Load-dependent piecewise control problem

Based the above approximation, the capability of MR dampers has been quantitative described. Due to the piecewise constant form of the constraints, the force controller can be designed without using the MPC (model predictive control) methods which are usually employed to handle nonlinear constraints and show poor real-time performance [27,28]. Further, considering the robust requirement mentioned above, the mature $H_\infty$ control techniques are more appropriate and practical. However, the constraints of origin-excluded partitions in system (4), which are asymmetric about zero (thus $q_{\mathrm{L}i} \neq -q_{\mathrm{U}i}$ when $i \in \zeta_1$), are difficult to be handled within the framework of $H_\infty$ control design. Therefore, a PWA controller is suggested in [26] as follows:

$$u = \mathbf{K}_i \mathbf{x} + d_i, \quad i \in \zeta \tag{5}$$

where the affine item is predesigned as that $d_i = (q_{\mathrm{L}i} + q_{\mathrm{U}i})/2$ to transform the asymmetric constraints to symmetric ones as follows:

$$|\mathbf{K}_i \mathbf{x}| \leqslant \bar{u}_{\max,i} \tag{6}$$

where $\bar{u}_{\max,i} = (q_{\mathrm{U}i} - q_{\mathrm{L}i})/2$. The feedback gain $\mathbf{K}_i$ plays a leading role in disturbance attenuation, constraint assurance and system stability.

Based on the above innovations on suspension model and controller style, the following control problem has been concerned in [26].

**Problem 1.** For a constant $m_{\mathrm{s}}$, define a global quadratic Lyapunov function (GQLF) as that $\mathbf{V}_{\mathrm{g}}(\mathbf{x}) = \mathbf{x}^{\mathrm{T}}\bar{\mathbf{P}}\mathbf{x}$. Then find a set of control gains $\mathbf{K}_i$ and a matrix $\bar{\mathbf{P}}$, such that the closed-loop system consisting of (4) and (5) is asymptotically stable, the $H_\infty$ norm from $w$ to $\mathbf{z}$ is less than a given scalar $\gamma$, and the constraints in (6) are satisfied when $\int_0^\infty w^{\mathrm{T}}(t)w(t)dt \leqslant w_{\max}$.

The resulted GQLF-based PWA-$H_\infty$ controller can guarantee the designed performance within the ability of MR dampers and the uniform $\bar{\mathbf{P}}$ will lead to a concise design process. However, by depicting the design schema of Problem 1 in Fig. 3(a), we can see that: (1) the GQLF ensures not only the state stabilities of possible switches (adjacent partitions) but also those of the impossible switches (nonadjacent partitions), and (2) the GQLF is employed to handle different load conditions and different constraints of every subsystem. Both of these aspects will lead to a conservative $\mathbf{K}_i$ which will limit the performance of MR dampers. As a contrast, Fig. 3(b) shows an ideal design schema where every partition has its own Lyapunov matrix and the time-varying property of the Lyapunov matrices will make control gains change with the load variation. To realize this schema, this paper considers a PDPQLF as follows

$$\mathbf{V}_{\mathrm{p}}(\mathbf{x}, m_{\mathrm{s}}) = \mathbf{x}^{\mathrm{T}}\mathbf{P}_i(m_{\mathrm{s}})\mathbf{x}. \tag{7}$$

Therefore, as a modification of Eq. (5), a following LDPWA controller will be designed:

$$u = \mathbf{K}_i(m_{\mathrm{s}})\mathbf{x} + d_i. \tag{8}$$

Continuous-time PWA systems declare that Lyapunov functions should be continuously differentiable [36], which is a strong requirement and is adverse to the conservatism reduction. Therefore, this paper will consider discrete-time systems. By choosing a suitable sampling interval, the closed-loop system consisting of (4) and (8) can be discretized as follows:

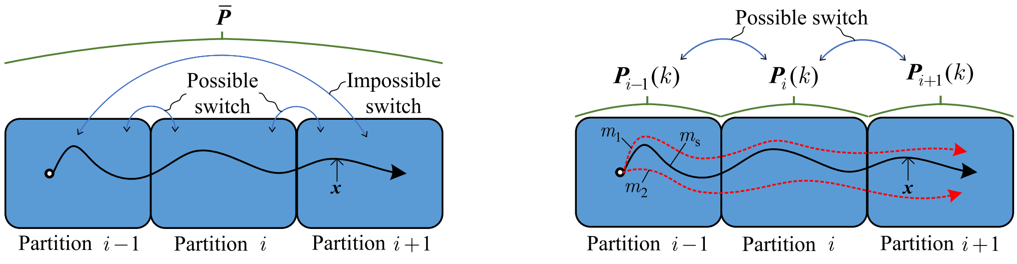

(a) (b)

**Fig. 3.** State transition and design schemas: (a) constant GQLF-based control; (b) time-varying PQLF-based control.

$$\begin{aligned}\mathbf{x}(k+1)&=\mathbf{\Theta}_i(m_s)\mathbf{x}(k)+\bar{\mathbf{W}}_i w(k)+\bar{\mathbf{B}}_i(m_s)d_i\\ \mathbf{z}(k)&=\mathbf{\Phi}_i(m_s)\mathbf{x}(k)+\bar{\mathbf{D}}_i(m_s)d_i\end{aligned} \tag{9}$$

where $\mathbf{\Theta}_i(m_s)=\bar{\mathbf{A}}_i(m_s)+\bar{\mathbf{B}}_i(m_s)\mathbf{K}_i(m_s)$ , $\mathbf{\Phi}_i(m_s)=\bar{\mathbf{C}}_i(m_s)+\bar{\mathbf{D}}_i(m_s)\mathbf{K}_i(m_s)$. The system matrices $\bar{\mathbf{A}}(m_s),\bar{\mathbf{B}}(m_s),\bar{\mathbf{C}}(m_s),\bar{\mathbf{D}}(m_s)$, and $\bar{\mathbf{W}}$ are the discrete-time forms of $\mathbf{A}_i(m_s),\mathbf{B}_i(m_s),\mathbf{C}_i(m_s),\mathbf{D}_i(m_s)$, and $\mathbf{W}_i$, respectively. Further, it is obvious that the load-dependent system matrices of the $i$-th subsystem in (9) satisfy that

$$\begin{bmatrix}\bar{\mathbf{A}}_i(m_s) & \bar{\mathbf{B}}_i(m_s)\\ \bar{\mathbf{C}}_i(m_s) & \bar{\mathbf{D}}_i(m_s)\end{bmatrix}=\sum_{n_i=1}^{2}\delta_{n_i}(m_s)\begin{bmatrix}\bar{\mathbf{A}}_{i,n_i} & \bar{\mathbf{B}}_{i,n_i}\\ \bar{\mathbf{C}}_{i,n_i} & \bar{\mathbf{D}}_{i,n_i}\end{bmatrix} \tag{10}$$

where $\delta_1(m_s)+\delta_2(m_s)=1;\bar{\mathbf{A}}_{i,1},\bar{\mathbf{B}}_{i,1},\bar{\mathbf{C}}_{i,1}$ and $\bar{\mathbf{D}}_{i,1}$ are constant matrices with $m_s=m_1;\bar{\mathbf{A}}_{i,2},\bar{\mathbf{B}}_{i,2},\bar{\mathbf{C}}_{i,2}$ and $\bar{\mathbf{D}}_{i,2}$ are those with $m_s=m_2$. Moreover, with the measurable $m_s,\delta_1(m_s)$ and $\delta_2(m_s)$ can be obtained as that:

$$\delta_1(m_s)=\frac{m_1(m_2-m_s)}{m_s(m_2-m_1)},\quad \delta_2(m_s)=\frac{m_2(m_s-m_1)}{m_s(m_2-m_1)}. \tag{11}$$

Therefore, the control problem concerned in this paper can be drawn as follows:

**Problem 2.** For time-varying $m_s$, find a set of load-dependent Lyapunov matrices $\mathbf{P}_i(m_s)$ for (7) and control gains $\mathbf{K}_i(m_s)$ for (8), such that system (9) is asymptotically stable with the given $H_\infty$ index $\gamma$ and the constraints in (6) are satisfied when $w$ is bounded by $w_{\max}$.

To facilitate the problem solving, some definitions and conditions are pre-specified. Specifically, when the states of system (9) transit from $\mathcal{R}_i$ to $\mathcal{R}_j$ at time $k$, we specify that the system is governed by the dynamics of the subsystem in $\mathcal{R}_i$ at that time. Let $\Omega$ represent the set of index pairs which denote the possible switches from one partition to itself or another partition, that is:

$$\Omega=\left\{(i,j)|\mathbf{x}(k)\in\mathcal{R}_i,\mathbf{x}(k+1)\in\mathcal{R}_j,i\in\zeta\right\}. \tag{12}$$

Further, the state regions $\mathcal{R}_i$ of origin-excluded partitions can be exactly described by following degenerate ellipsoids:

$$\mathcal{L}_i=\{\mathbf{x}(k)|\|\mathbf{F}_i\mathbf{x}(k)+f_i\|\leqslant 1\},\quad i\in\zeta_1 \tag{13}$$

where $\mathbf{F}_i=2\mathbf{e}/(p_{Ui}-p_{Li}),f_i=-(p_{Ui}+p_{Li})/(p_{Ui}-p_{Li})$, and $\mathbf{e}=[0\ 0\ 1\ \ -1]$.

## 3. Controller design

In this section, we focus on solving the problems derived in last section with linear matrix inequalities (LMIs).

### 3.1. Design of the GQLF-based PWA-$H_\infty$ Controller

For Problem 1, the constant control gains in (5) can be obtained through the following theorem.

**Theorem 1.** *An admissible set of control gains $\mathbf{K}_i$ in (5) exists such that the requirements in Problem 1 are satisfied, if there exist matrices $\bar{\mathbf{Q}}^{\mathrm{T}}=\bar{\mathbf{Q}}>0,\mathbf{Y}_i>0$, and scalars $\lambda_i<0$, such that the following LMIs hold:*

$$\begin{bmatrix}\mathbf{\Xi}_i & \star\\ \mathbf{C}_i\bar{\mathbf{Q}}+\mathbf{D}_i\mathbf{Y}_i & -\mathbf{I}\end{bmatrix}<0,\quad i\in\zeta_0, \tag{14a}$$

$$\begin{bmatrix}\mathbf{\Xi}_i+\lambda_i\mathbf{B}_i d_i(\mathbf{B}_i d_i)^{\mathrm{T}} & \star & \star\\ \mathbf{C}_i\bar{\mathbf{Q}}+\mathbf{D}_i\mathbf{Y}_i & -\mathbf{I} & \star\\ \left(\lambda_i\mathbf{B}_i d_i f_i^{\mathrm{T}}+\bar{\mathbf{Q}}\mathbf{F}_i^{\mathrm{T}}\right)^{\mathrm{T}} & 0 & -\lambda_i\left(1-f_i^2\right)\end{bmatrix}<0,\quad i\in\zeta_1, \tag{14b}$$

$$\begin{bmatrix}\frac{\gamma^{-2}\bar{u}_{\max,i}}{w_{\max}} & \star\\ \mathbf{Y}_i^{\mathrm{T}} & \bar{\mathbf{Q}}\end{bmatrix}\geqslant 0,\quad i\in\zeta \tag{14c}$$

*where $\mathbf{\Xi}_i=\bar{\mathbf{Q}}\mathbf{A}_i^{\mathrm{T}}+\mathbf{A}_i\bar{\mathbf{Q}}+\mathbf{Y}_i^{\mathrm{T}}\mathbf{B}_i^{\mathrm{T}}+\mathbf{B}_i\mathbf{Y}_i+\gamma^{-2}\mathbf{W}_i\mathbf{W}_i^{\mathrm{T}},\mathbf{A}_i,\mathbf{B}_i,\mathbf{C}_i,\mathbf{D}_i$ are constant system matrices, $\mathbf{I}$ is an identity matrix and $\star$ denotes the items induced by matrix symmetry. Moreover, the constant gains and the global Lyapunov matrix can be obtained as that:*

$$\mathbf{K}_i=\mathbf{Y}_i\bar{\mathbf{Q}}^{-1},\quad \bar{\mathbf{P}}=\bar{\mathbf{Q}}^{-1},\quad i\in\zeta. \tag{15}$$

**Proof.** Derivation of this theorem has been given in [26]. □

### 3.2. Design of the PDPQLF-based LDPWA-$H_\infty$ Controller

For Problem 2, the time-varying control gains in (8) can be obtained through the following theorem.

**Theorem 2.** *For all* $(i,j) \in \Omega, n_i \in \{1,2\}$ *and* $n_j \in \{1,2\}$, *an admissible set of gains* $\mathbf{K}_i(m_s)$ *in* (8) *exists such that the requirements in* Problem 2 *are satisfied, if there exist matrices:* $\mathbf{Q}_{i,n_i}^{\mathrm{T}} = \mathbf{Q}_{i,n_i} > 0, \mathbf{Q}_{j,n_i}^{\mathrm{T}} = \mathbf{Q}_{j,n_i} > 0, \mathbf{G}_{i,n_i}, \mathbf{R}_{i,n_i}$ *and scalars:* $\eta_i > 0, \mu_i > 0$, *such that the following LMIs hold:*

$$\begin{bmatrix} -\gamma^2\mathbf{I} & \star & \star & \star \\ \bar{\mathbf{W}}_i & -\mathbf{Q}_{j,n_j} & \star & \star \\ 0 & 0 & -\mathbf{I} & \star \\ 0 & \mathbf{\Psi}_{i,n_i} & \mathbf{\Pi}_{i,n_i} & \mathbf{\Upsilon}_{i,n_i} \end{bmatrix} < 0, \quad i \in \zeta_0, \tag{16a}$$

$$\begin{bmatrix} -\gamma^2\mathbf{I} & \star & \star & \star & \star \\ \bar{\mathbf{W}}_i & \mathbf{\Lambda}_{ij,n_in_j} & \star & \star & \star \\ 0 & 0 & -\mathbf{I} & \star & \star \\ 0 & \eta_i f_i \left(\bar{\mathbf{B}}_{i,n_i} d_i\right)^{\mathrm{T}} & 0 & -\eta_i\left(f_i^2 - 1\right) & \star \\ 0 & \mathbf{\Psi}_{i,n_i} & \mathbf{\Pi}_{i,n_i} & -\mathbf{G}_{i,n_i}^{\mathrm{T}}\mathbf{F}_i^{\mathrm{T}} & \mathbf{\Upsilon}_{i,n_i} \end{bmatrix} < 0, \quad i \in \zeta_1, \tag{16b}$$

$$\begin{bmatrix} \frac{\bar{u}_{\max,i}^2}{\gamma^2 w_{\max}} \mathbf{\Upsilon}_{i,n_i} & \star \\ \mathbf{R}_{i,n_i} & -\mathbf{I} \end{bmatrix} \leqslant 0, \quad i \in \zeta_0, \tag{17a}$$

$$\begin{bmatrix} \frac{\bar{u}_{\max,i}^2}{\gamma^2 w_{\max}} \mathbf{\Upsilon}_{i,n_i} & \star & \star \\ \mathbf{R}_{i,i_n} & -\mathbf{I} & \star \\ \mathbf{F}_i\mathbf{G}_{i,i_n} & 0 & -\mu_i\left(f_i^2 - 1\right) \end{bmatrix} \leqslant 0, \quad i \in \zeta_1 \tag{17b}$$

*where*

$$\begin{aligned} \mathbf{\Psi}_{i,n_i} &= \left(\bar{\mathbf{A}}_{i,n_i}\mathbf{G}_{i,n_i} + \bar{\mathbf{B}}_{i,n_i}\mathbf{R}_{i,n_i}\right)^{\mathrm{T}}, \\ \mathbf{\Pi}_{i,n_i} &= \left(\bar{\mathbf{C}}_{i,n_i}\mathbf{G}_{i,n_i} + \bar{\mathbf{D}}_{i,n_i}\mathbf{R}_{i,n_i}\right)^{\mathrm{T}}, \\ \mathbf{\Upsilon}_{i,n_i} &= \mathbf{Q}_{i,n_i} - \mathbf{G}_{i,n_i} - \mathbf{G}_{i,n_i}^{\mathrm{T}}, \\ \boldsymbol{\lambda}_{ij,n_in_j} &= -\mathbf{Q}_{j,n_j} - \eta_i\bar{\mathbf{B}}_{i,n_i}d_i\left(\bar{\mathbf{B}}_{i,n_i}d_i\right)^{\mathrm{T}}. \end{aligned}$$

*Moreover, the load-dependent control gains and Lyapunov matrices can be obtained as that:*

$$\mathbf{K}_i(m_s) = \sum_{n_i=1}^{2} \delta_{n_i}(m_s)\mathbf{R}_{i,n_i}\mathbf{G}_{i,n_i}^{-1}, \tag{18a}$$

$$\mathbf{P}_i(m_s) = \sum_{n_i=1}^{2} \delta_{n_i}(m_s)\mathbf{Q}_{i,n_i}^{-1}, \ i \in \zeta. \tag{18b}$$

**Proof.** As the item $\bar{\mathbf{D}}_i(m_s)d_i$ in (9) affects neither the system stability nor the $H_\infty$ performance, a sufficient condition for the satisfaction of the requirements on system stability and disturbance attenuation in Problem 2 is that the following inequality holds:

$$\mathbf{V}_{\mathrm{p}}(\mathbf{x}(k+1)) - \mathbf{V}_{\mathrm{p}}(\mathbf{x}(k)) + \tilde{\mathbf{z}}^{\mathrm{T}}(k)\tilde{\mathbf{z}}(k) - \gamma^2 w^{\mathrm{T}}(k)w(k) < 0 \tag{19}$$

where $\tilde{\mathbf{z}}(k) = \mathbf{z}(k) - \bar{\mathbf{D}}_i(m_s)d_i$. To facilitate the derivation, the time instant $k$ and the time-varying parameter $m_s$ will be omitted in the following.

Substitute (9) into (19), the following inequality can be obtained:

$$\left[\mathbf{\Theta}_i\mathbf{x} + \bar{\mathbf{W}}_i w + \bar{\mathbf{B}}_i d_i\right]^{\mathrm{T}}\mathbf{P}_j\left[\mathbf{\Theta}_i\mathbf{x} + \bar{\mathbf{W}}_i w + \bar{\mathbf{B}}_i d_i\right] - \mathbf{x}^{\mathrm{T}}\mathbf{P}_i\mathbf{x} + \mathbf{x}^{\mathrm{T}}\mathbf{\Phi}_i^{\mathrm{T}}\mathbf{\Phi}_i\mathbf{x} - \gamma^2 w^{\mathrm{T}} w < 0. \tag{20}$$

Inequality (20) can be rewritten in the following matrix form:

$$\begin{bmatrix} \mathbf{x} \\ w \\ 1 \end{bmatrix}^{\mathrm{T}} \left( \begin{bmatrix} \mathbf{\Phi}_i \\ 0 \\ 0 \end{bmatrix} (\bigstar) + \begin{bmatrix} \mathbf{\Theta}_i \\ \bar{\mathbf{W}}_i \\ \bar{\mathbf{B}}_i d_i \end{bmatrix} \mathbf{P}_j (\bigstar) + \begin{bmatrix} -\mathbf{P}_i & \bigstar & \bigstar \\ 0 & -\gamma^2 \mathbf{I} & \bigstar \\ 0 & 0 & 0 \end{bmatrix} \right) \begin{bmatrix} \mathbf{x} \\ w \\ 1 \end{bmatrix} \leqslant 0. \tag{21}$$

For $i \in \zeta_1$, the partition information expressed in (13) can be induced into (21) by using the S-procedure. Further, by using Schur complement twice for (21), we can get the following inequality:

$$\begin{bmatrix} -\mathbf{P}_i - \lambda_i \mathbf{F}_i^{\mathrm{T}} \mathbf{F}_i & \bigstar & \bigstar & \bigstar & \bigstar \\ 0 & -\gamma^2 \mathbf{I} & \bigstar & \bigstar & \bigstar \\ -\lambda_i f_i \mathbf{F}_i & 0 & -\lambda_i \left( f_i^2 - 1 \right) & \bigstar & \bigstar \\ \mathbf{\Theta}_i & \bar{\mathbf{W}}_i & \bar{\mathbf{B}}_i d_i & -\mathbf{P}_j^{-1} & \bigstar \\ \mathbf{\Phi}_i & 0 & 0 & 0 & -\mathbf{I} \end{bmatrix} \leqslant 0 \tag{22}$$

where $\lambda_i$ is a positive scalar. Pre- and post-multiplying (22) by

$$\boldsymbol{\theta}_j = \begin{bmatrix} 0 & \mathbf{I} & 0 & 0 & 0 \\ 0 & 0 & 0 & \mathbf{P}_j & 0 \\ 0 & 0 & 0 & 0 & \mathbf{I} \\ \mathbf{I} & 0 & 0 & 0 & 0 \\ 0 & 0 & \mathbf{I} & 0 & 0 \end{bmatrix}$$

and $\boldsymbol{\theta}_j^{\mathrm{T}}$ respectively, we obtain that:

$$\begin{bmatrix} -\gamma^2 \mathbf{I} & \bigstar & \bigstar & \bigstar & \bigstar \\ \mathbf{P}_j \bar{\mathbf{W}}_i & -\mathbf{P}_j & \bigstar & \bigstar & \bigstar \\ 0 & 0 & -\mathbf{I} & \bigstar & \bigstar \\ 0 & \mathbf{\Theta}_i^{\mathrm{T}} \mathbf{P}_j & \mathbf{\Phi}_i^{\mathrm{T}} & -\mathbf{P}_i - \lambda_i \mathbf{F}_i^{\mathrm{T}} \mathbf{F}_i & \bigstar \\ 0 & \left( \bar{\mathbf{B}}_i d_i \right)^{\mathrm{T}} \mathbf{P}_j & 0 & -\lambda_i f_i^{\mathrm{T}} \mathbf{F}_i & -\lambda_i \left( f_i^2 - 1 \right) \end{bmatrix} \leqslant 0. \tag{23}$$

Using the Schur complement again, inequality (23) can be transformed into that:

$$\begin{bmatrix} -\gamma^2 \mathbf{I} & \bigstar & \bigstar & \bigstar \\ \mathbf{P}_j \bar{\mathbf{W}}_i & -\mathbf{P}_j & \bigstar & \bigstar \\ 0 & 0 & -\mathbf{I} & \bigstar \\ 0 & \mathbf{\Theta}_i^{\mathrm{T}} \mathbf{P}_j & \mathbf{\Phi}_i^{\mathrm{T}} & -\mathbf{P}_i - \lambda_i \mathbf{F}_i^{\mathrm{T}} \mathbf{F}_i \end{bmatrix} - \begin{bmatrix} 0 \\ \mathbf{P}_j \bar{\mathbf{B}}_i d_i \\ 0 \\ -\lambda_i \mathbf{F}_i^{\mathrm{T}} f_i \end{bmatrix} \lambda_i^{-1} \left( 1 - f_i^2 \right)^{-1} (\bigstar) \leqslant 0. \tag{24}$$

As that $\left(1 - f_i^2\right)^{-1} = 1 + f_i \left(1 - f_i^2\right)^{-1} f_i$, expression (24) can be equally written as that:

$$\begin{bmatrix} -\gamma^2 \mathbf{I} & \bigstar & \bigstar & \bigstar \\ \mathbf{P}_j \bar{\mathbf{W}}_i & \varphi_{ij} & \bigstar & \bigstar \\ 0 & 0 & -\mathbf{I} & \bigstar \\ 0 & \mathbf{\Theta}_i^{\mathrm{T}} \mathbf{P}_j & \mathbf{\Phi}_i^{\mathrm{T}} & -\mathbf{P}_i \end{bmatrix} - \begin{bmatrix} 0 \\ \lambda_i^{-1} \mathbf{P}_j \bar{\mathbf{B}}_i d_i f_i \\ 0 \\ -\mathbf{F}_i^{\mathrm{T}} \end{bmatrix} \lambda_i \left( 1 - f_i^2 \right)^{-1} (\bigstar) \leqslant 0 \tag{25}$$

where $\varphi_{ij} = -\mathbf{P}_j - \lambda_i^{-1} \mathbf{P}_j \bar{\mathbf{B}}_i d_i \left( \bar{\mathbf{B}}_i d_i \right)^{\mathrm{T}} \mathbf{P}_j$. Using Schur complement for (25), we can obtain that:

$$\begin{bmatrix} -\gamma^2 \mathbf{I} & \bigstar & \bigstar & \bigstar & \bigstar \\ \mathbf{P}_j \bar{\mathbf{W}}_i & \varphi_{ij} & \bigstar & \bigstar & \bigstar \\ 0 & 0 & -\mathbf{I} & \bigstar & \bigstar \\ 0 & \mathbf{\Theta}_i^{\mathrm{T}} \mathbf{P}_j & \mathbf{\Phi}_i^{\mathrm{T}} & -\mathbf{P}_i & \bigstar \\ 0 & \lambda_i^{-1} f_i d_i \bar{\mathbf{B}}_i^{\mathrm{T}} \mathbf{P}_j & 0 & -\mathbf{F}_i & -\lambda_i^{-1} \left( f_i^2 - 1 \right) \end{bmatrix} \leqslant 0. \tag{26}$$

Pre- and post-multiplying (26) by

$$\psi_{ij} = diag \left\{ \mathbf{I}, \quad \mathbf{P}_j^{-1}, \quad \mathbf{I}, \quad \begin{bmatrix} 0 & \mathbf{I} \\ \mathbf{P}_i^{-1} & 0 \end{bmatrix} \right\}$$

and $\psi_{ij}^{\mathrm{T}}$ respectively, and then applying $\mathbf{Q}_i = \mathbf{P}_i^{-1}, \mathbf{Q}_j = \mathbf{P}_j^{-1}$ and $\eta_i = \lambda_i^{-1}$, we can obtain that:

$$\begin{bmatrix} -\gamma^2\mathbf{I} & \star & \star & \star & \star \\ \bar{\mathbf{W}}_i & -\mathbf{Q}_j - \eta_i\bar{\mathbf{B}}_i d_i\left(\bar{\mathbf{B}}_i d_i\right)^{\mathrm{T}} & \star & \star & \star \\ 0 & 0 & -\mathbf{I} & \star & \star \\ 0 & \eta_i f_i d_i^{\mathrm{T}}\bar{\mathbf{B}}_i^{\mathrm{T}} & 0 & -\lambda_i^{-1}\left(f_i^2 - 1\right) & \star \\ 0 & \mathbf{Q}_i\boldsymbol{\Theta}_i^{\mathrm{T}} & \mathbf{Q}_i\boldsymbol{\Phi}_i^{\mathrm{T}} & -\mathbf{Q}_i\mathbf{F}_i & -\mathbf{Q}_i \end{bmatrix} \leqslant 0. \tag{27}$$

Then, according to Lemma 1 given in the Appendix, we can obtain that a sufficient condition that guarantees (27) is that there exists matrix $\mathbf{G}_i(m_s)$ such that the following inequality holds:

$$\begin{bmatrix} -\gamma^2\mathbf{I} & \star & \star & \star & \star \\ \bar{\mathbf{W}}_i & \boldsymbol{\lambda}_{ij} & \star & \star & \star \\ 0 & 0 & -\mathbf{I} & \star & \star \\ 0 & \eta_i f_i\left(\bar{\mathbf{B}}_i d_i\right)^{\mathrm{T}} & 0 & -\eta_i\left(1f_i^2 - 1\right) & \star \\ 0 & \boldsymbol{\Psi}_i & \boldsymbol{\Pi}_i & -\mathbf{G}_i^{\mathrm{T}}\mathbf{F}_i^{\mathrm{T}} & \boldsymbol{\Upsilon}_i \end{bmatrix} \leqslant 0 \tag{28}$$

where

$$\begin{aligned} \boldsymbol{\Psi}_i &= \left(\bar{\mathbf{A}}_i\mathbf{G}_i + \bar{\mathbf{B}}_i\mathbf{R}_i\right)^{\mathrm{T}}, \quad \boldsymbol{\Pi}_i = \left(\bar{\mathbf{C}}_i\mathbf{G}_i + \bar{\mathbf{D}}_i\mathbf{R}_i\right)^{\mathrm{T}}, \\ \boldsymbol{\Upsilon}_i &= \mathbf{Q}_i - \mathbf{G}_i - \mathbf{G}_i^{\mathrm{T}}, \quad \boldsymbol{\lambda}_{ij} = -\mathbf{Q}_j - \eta_i\bar{\mathbf{B}}_i d_i\left(\bar{\mathbf{B}}_i d_i\right)^{\mathrm{T}}, \end{aligned}$$

and $\mathbf{R}_i = \mathbf{K}_i\mathbf{G}_i$. Therefore, in the following, we just need to prove that (16b) can satisfy (28).

Consider a fixed pair $(i,j)$, firstly, for each $n_i$, multiply inequalities (16b) labeled with $n_j$ with $\delta_{n_j}$ and sum. Then, multiply the inequalities labeled with $n_i$ with $\delta_{n_i}$ and sum. Due to that $\delta_1 + \delta_2 = 1$, we can finally obtain (28) once the matrices $\mathbf{G}_i$ and $\mathbf{R}_i$ satisfy that:

$$\mathbf{G}_i(m_s) = \sum_{n_i=1}^{2}\delta_{n_i}(m_s)\mathbf{G}_{i,n_i}, \ \mathbf{R}_i(m_s) = \sum_{n_i=1}^{2}\delta_{n_i}(m_s)\mathbf{R}_{i,n_i}$$

and $\mathbf{K}_i, \mathbf{P}_i$ satisfy (18). Similarly, for the origin-included partition $(i \in \zeta_0)$, we can obtain (16a) without considering the ellipsoidal state information.

In the following, the LMIs that guarantee the control constraints will be derived. By summing (19) from 0 to $\infty$, we can obtain that:

$$\mathbf{V}_{\mathrm{p}}(\mathbf{x}(k)) + \sum_{k=0}^{\infty}\|\tilde{\mathbf{z}}^{\mathrm{T}}(k)\tilde{\mathbf{z}}(k)\| \leqslant \gamma^2\sum_{k=0}^{\infty}w^{\mathrm{T}}(k)w(k). \tag{29}$$

Due to the bounded disturbance energy, we can further obtain from (29) that:

$$\mathbf{V}_{\mathrm{p}}(\mathbf{x}(k)) \leqslant \gamma^2 w_{\max}. \tag{30}$$

Further, for the origin-excluded partitions, (30) and (13) can be induced into (6) by using the S-procedure to obtain a sufficient condition which guarantees the control constraints as that: there exist positive scalars $\alpha_i$ and $\beta_i$ such that the following inequality holds:

$$\left(\mathbf{x}^{\mathrm{T}}\mathbf{K}_i^{\mathrm{T}}\mathbf{K}_i\mathbf{x} - \bar{u}_{\max,i}^2\right) - \alpha_i\left(\mathbf{V}_{\mathrm{p}}(\mathbf{x}) - \gamma^2 w_{\max}\right) - \beta_i\begin{bmatrix}\mathbf{x}\\1\end{bmatrix}^{\mathrm{T}}\begin{bmatrix}\mathbf{F}_i^{\mathrm{T}}\mathbf{F}_i & \star \\ f_i\mathbf{F}_i & f_i^2 - 1\end{bmatrix}\begin{bmatrix}\mathbf{x}\\1\end{bmatrix} \leqslant 0. \tag{31}$$

By assigning $\alpha_i$ as $\bar{u}_{\max,i}^2/(\gamma^2 w_{\max})$ and using the Schur complement, (31) can be reformed as:

$$\begin{bmatrix} -\frac{\bar{u}_{\max,i}^2}{\gamma^2 w_{\max}}\mathbf{P}_i & \star & \star \\ \mathbf{K}_i & -\mathbf{I} & \star \\ \mathbf{F}_i & 0 & -\beta_i^{-1}\left(f_i^2 - 1\right) \end{bmatrix} \leqslant 0. \tag{32}$$

Pre- and post-multiplying (32) with $\tilde{\theta}_i = diag\left\{\mathbf{G}_i^{\mathrm{T}}, \mathbf{I}, \mathbf{I}\right\}$ and $\tilde{\theta}_i^{\mathrm{T}}$, respectively, and applying $\mu_i = \beta_i^{-1}, \mathbf{Q}_i = \mathbf{P}_i^{-1}$ and $\mathbf{R}_i = \mathbf{K}_i\mathbf{G}_i$, we can obtain that:

$$\begin{bmatrix} -\frac{\bar{u}_{\max,i}^2}{\gamma^2 w_{\max}}\mathbf{G}_i^{\mathrm{T}}\mathbf{Q}_i^{-1}\mathbf{G}_i & \star & \star \\ \mathbf{R}_i & -\mathbf{I} & \star \\ \mathbf{F}_i\mathbf{G}_i & 0 & -\mu_i\left(f_i^2 - 1\right) \end{bmatrix} \leqslant 0. \tag{33}$$

Due to that $\mathbf{Q}_i - \mathbf{G}_i - \mathbf{G}_i^{\mathrm{T}} \geqslant -\mathbf{G}_i^{\mathrm{T}}\mathbf{Q}_i^{-1}\mathbf{G}_i$, a sufficient condition that guarantee (33) is that:

$$\begin{bmatrix} \frac{\bar{u}^2_{\max,i}}{\gamma^2 w_{\max}}\boldsymbol{\Upsilon}_i & \star & \star \\ \mathbf{R}_i & -\mathbf{I} & \star \\ \mathbf{F}_i\mathbf{G}_i & 0 & -\mu_i\left(f_i^2 - 1\right) \end{bmatrix} \leqslant 0. \tag{34}$$

Further, by using the same method which derives (28) from (16b), we can prove that (17b) guarantees (34). In a similar way, inequality (17aa) can be obtained for the origin-included partition without considering the ellipsoidal state information. The proof is completed. □

**Remark 5.** For Theorem 1, the number of LMIs that should be optimized together is $2N$, while for Theorem 2, the optimization complexity is related to both the partition number and the element number in $\Omega$. For the division method given in Section 2, the number of switch pair is $3N - 2$. Further, due to the load variation, the number of possible switches that corresponds to each $(i,j)$ will be $n_i n_j$. Therefore, the number of LMIs expressed in (16) and (17) that should be solved together is $2n_i n_j(3N - 2)$.

**Remark 6.** Besides the application in semi-active suspension control, Theorem 2 is applicable to general piecewise linear systems with asymmetrical constraints and time-varying parameters.

## 4. Simulation analysis

### 4.1. Simulation environment and control algorithms

The parameters of the QoV model are given in Table 1. Additionally, three different sprung mass values $m_1, \bar{m}$ and $m_2$, which respectively correspond to minimal, nominal and maximal load conditions, are chosen.

### 4.1.1. MR damper models

Various models had been proposed to represent the complex nonlinearities of the MR damper, for example, Bingham model [37], Bouc-Wen model [38], modified Bouc-Wen model [39], ANFIS model [40] and so on. The Bingham model is simple, but the hysteresis cannot be adequately described. Therefore, this model is only employed in situations when there is a significant need for a simple model. The Bouc-Wen model or its modified form can accurately represent the nonlinearities of MR dampers. However, the model complexity is unavoidably increased with an extended number of model parameters which may impose difficulties in the identification. Additionally, Bouc-Wen models can only display the normal character of MR dampers (from $\dot{z}_{\mathrm{def}}$ and $I$ to $F$), which will inevitably lead to the additional modeling work on the inverse character (from $F$ and $\dot{z}_{\mathrm{def}}$ to $I$). The ANFIS model can accurately describe the normal and inverse characteristics, but requires a large amount of test data. Considering the above aspects, a hyperbolic tangent function based damper model from [41] is employed in this paper with the following expression:

$$F = c_0\dot{z}_{\mathrm{def}} + k_0 z_{\mathrm{def}} + y_{\mathrm{mr}} I \tanh(c_1\dot{z}_{\mathrm{def}} + k_1 z_{\mathrm{def}}) \tag{35}$$

where $I$ is the electric current input, $y_{\mathrm{mr}}$ is a proportional rate of damping force per ampere over the deflection velocity, $c_0$ is a linear viscous damping coefficient, $k_0$ is a linear stiffness coefficient, $c_1$ and $k_1$ are hysteresis coefficients related to the deflection displacement and velocity, respectively. Since every parameter has a specific physical meaning, expression (35) is a phenomenological model. Accordingly, the mechanical constitution of this model is depicted in Fig. 4(a). From (35), we can see that there are only five parameters to be identified, and the model structure is relatively simple such that an inverse damper model can be easily obtained as follows:

$$I = (F - c_0\dot{z}_{\mathrm{def}} - k_0 z_{\mathrm{def}})/(y_{\mathrm{mr}} \tanh(c_1\dot{z}_{\mathrm{def}} + k_1 z_{\mathrm{def}})). \tag{36}$$

Models (35) and (36) can clearly describe the normal and inverse characters of MR dampers respectively, notably the hysteresis and bilinear nonlinearities [42]. However, the model accuracy is limited, especially for the complex condition with a wide range of vibration frequency. Nevertheless, considering the trade-off between accuracy and complexity, model (35) is

**Table 1**
QoV model parameters.

| $m_s$ | | | $m_u$ | $k_s$ | $c_s$ | $k_t$ |
|---|---|---|---|---|---|---|
| $m_1$ | $\bar{m}$ | $m_2$ | 75 kg | 27kN/m | 400Ns/m | 400kN/m |
| 350 kg | 450 kg | 550 kg | | | | |

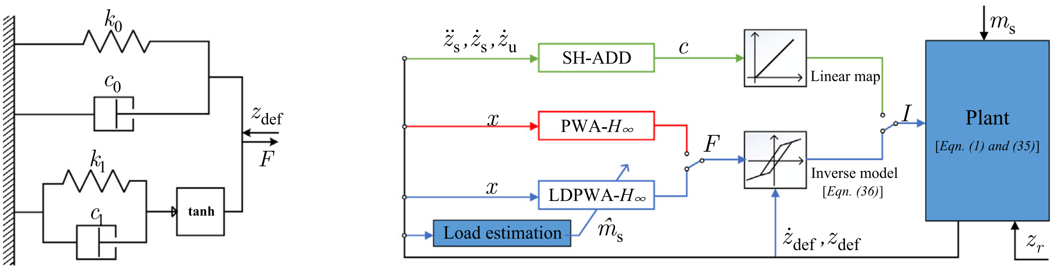

(a) (b)

**Fig. 4.** (a) Mechanical structure of hyperbolic tangent function based MR models; (b) Application schemas of damping force controllers.

still widely used for the control design purpose [30], and will be used in this paper for the evaluation of damping force controllers. If rich damper test data can be obtained, and the computing power of hardware control unit is strong enough, the inverse ANFIS model can also be utilized to achieve higher force tracking accuracy. In this paper, the parameters in (35) are identified based on the test data of a real MR damper from the FAW-Tokico corporation. The resulted parameter values are that:

$$c_0 = 810.78, \quad c_1 = 5.78, \quad k_0 = 620.79, \quad k_1 = 20, \quad y_{\rm mr} = 1200,$$

and the electric current range is that $I \in [0\ \text{A}, 3\ \text{A}]$.

### 4.1.2. Control algorithms

To get insight into the performance of the LDPWA-$H_\infty$ algorithm, this paper will simultaneously present the simulations of the PWA-$H_\infty$ algorithm and a classical semi-active algorithm namely SH-ADD. Application schemas of the three algorithms are shown in Fig. 4(b) where the plant is simulated by the interaction of expressions (1) and (35). Further, some preferences about the three algorithms are given below.

(1) PWA-$H_\infty$/LDPWA-$H_\infty$: According to the identified MR damper model and the approximation method given in [26], the velocity bounds and the force constraints of each partition for the design of PWA and LDPWA $H_\infty$ algorithms are listed in Table 2. In this paper, the partition number of $N = 9$ with $m_{\rm pre} = m_{\rm pst1} = m_{\rm pst2} = 3$ is considered (Detailed analysis on the influence of the partition number can be referred in [26]). Further, the control gains of these two algorithms are obtained by solving the LMI optimization problems given in Theorems 1 and 2, respectively. In this paper, the LMI problems are handled by a commercial solver named MOSEK [43]. To compare the two algorithms fairly, a common set of weighting coefficients are chosen as that $\rho_1 = 10, \rho_2 = 0.1$ and $\rho_3 = 10$. As PWA-$H_\infty$ algorithm can only concern the constant load, the nominal load value will be used for the controller design. While for LDPWA-$H_\infty$ algorithm, as shown in Fig. 4(b), we assume that an accurate load estimation module is employed, thus $\hat{m}_s = m_{\rm s}$. Additionally, the parameters $w_{\max}$ and $\gamma$, which should be pre-specified for the design, will be treated as adjustable parameters in this paper.

(2) SH-ADD: This is an effective comfort-oriented algorithm for semi-active suspensions [44]. Compared with the famous skyhook method, SH-ADD algorithm can reduce the vertical body acceleration in a wider frequency range. The algorithm can be expressed in a bang-bang form as follows:

$$c = \begin{cases} c_{\min}, & \text{if } \left[\left(\ddot{z}_{\rm s} - \kappa\dot{z}_{\rm s}^2\right) \leqslant 0 \cap \dot{z}_{\rm s}(\dot{z}_{\rm s} - \kappa\dot{z}_{\rm u}) > 0\right] \cup \left[\left(\ddot{z}_{\rm s} - \kappa\dot{z}_{\rm s}^2\right) \leqslant 0 \cap \dot{z}_{\rm s}(\dot{z}_{\rm s} - \kappa\dot{z}_{\rm u}) > 0\right] \\ c_{\max}, & \text{otherwise} \end{cases} \tag{37}$$

**Table 2**
Parameters of system piecewise approximation.

| | | | | | | | | |
|---|---|---|---|---|---|---|---|---|
| Velocity bounds (unit: m/s) | | | | | | | | |
| $p_{\rm L1}$ | $p_{\rm L2}$ | $p_{\rm L3}$ | $p_{\rm L4}$ | $p_{\rm L5}$ | $p_{\rm L6}$ | $p_{\rm L7}$ | $p_{\rm L8}$ | $p_{\rm L9}$ |
| -1.60 | −1.20 | −0.80 | −0.40 | −0.13 | 0.13 | 0.40 | 0.80 | 1.20 |
| $p_{\rm U1}$ | $p_{\rm U2}$ | $p_{\rm U3}$ | $p_{\rm U4}$ | $p_{\rm U5}$ | $p_{\rm U6}$ | $p_{\rm U7}$ | $p_{\rm U8}$ | $p_{\rm U9}$ |
| -1.20 | −0.80 | −0.40 | −0.13 | 0.13 | 0.40 | 0.80 | 1.20 | 1.60 |
| Force bounds (unit: kN) | | | | | | | | |
| $q_{\rm L1}$ | $q_{\rm L2}$ | $q_{\rm L3}$ | $q_{\rm L4}$ | $q_{\rm L5}$ | $q_{\rm L6}$ | $q_{\rm L7}$ | $q_{\rm L8}$ | $q_{\rm L9}$ |
| -4.88 | −4.54 | −4.19 | −3.84 | −0.50 | −1.07 | 0.32 | 0.66 | 0.98 |
| $q_{\rm U1}$ | $q_{\rm U2}$ | $q_{\rm U3}$ | $q_{\rm U4}$ | $q_{\rm U5}$ | $q_{\rm U6}$ | $q_{\rm U7}$ | $q_{\rm U8}$ | $q_{\rm U9}$ |
| -0.95 | −0.62 | −0.26 | 1.14 | 0.50 | 3.96 | 4.28 | 4.59 | 4.92 |

where $c$ is the damping coefficient and $\kappa$ is a design parameter which is set as 121. As SH-ADD algorithm concerns none of the actuator nonlinearity, a linear relationship between $c$ and the electric current is adopted in Fig. 4, thus $c_{\min} \rightarrow I_{\min}$ and $c_{\max} \rightarrow I_{\max}$. In this paper, SH-ADD algorithm will act as a representation of bang-bang controllers.

### 4.2. Conservatism analysis and parameter selection

In this subsection, the conservatism of PWA and LDPWA $H_\infty$ algorithms will be evaluated from two aspects: (1) feasibility of the corresponding LMI optimization problems; (2) performance of the closed-loop systems. Since both two aspects are highly related to the choice of parameters $w_{\max}$ and $\gamma$, a principle for the parameter selection will also be derived.

#### 4.2.1. Feasibility of LMI optimization problems

The feasibility of the LMI optimization problems given by Theorems 1 and 2 will be tested under different values of $w_{\max}$ and $\gamma$. In this paper, the ranges of $w_{\max}$ and $\gamma$ are chosen as (0.0001, 10000) and (0, 80), respectively. Then, by setting the intervals as that $\log_{10} w_{\max} = 0.1$ and $\gamma = 1$, the feasibility results of 6400 parameter pairs defined as $(w_{\max}, \gamma)$ are summarized in Fig. 5. Obviously, the feasible parameter range of LDPWA-$H_\infty$ algorithm is bigger than that of PWA-$H_\infty$ algorithm. Specifically, for PWA-$H_\infty$ algorithm, a small $\gamma$ or a big $w_{\max}$ both lead to unfeasible results. However, for LDPWA-$H_\infty$ algorithm, the corresponding LMI problem is feasible under almost all the tested parameters except that $\gamma$ is too small. Therefore, the above results also indicate that the complex form of Theorem 2 does not affect its feasibility. In addition, the resulted LDPWA-$H_\infty$ algorithm can theoretically handle more severe disturbance.

#### 4.2.2. Performance of closed-loop systems

Furthermore, the influence of parameters on suspension performance will be analyzed through closed-loop simulations. As a smaller $\gamma$ indicates better disturbance attenuation performance, only the feasible parameter pairs with the minimal $\gamma$ for each $w_{\max}$ will be evaluated here. In Fig. 5, these pairs make up the sets $\Gamma_1$ and $\Gamma_2$ for PWA and LDPWA $H_\infty$ algorithms, respectively. Thus, each $w_{\max}$ in $\Gamma_i$ corresponds to a control gain. To concentrate on the conservatism resulted from different design processes rather than outer conditions, a nominal load condition is simulated here and the vehicle is supposed to be running on a class C road which is suggested by the international organization for standardization (ISO) with a speed of 50 km/h. The generation of this road profile can be referred in [45]. After running the simulation under different control gains, the root-mean-square (RMS) values of response signals $\ddot{z}_s, z_u - z_r$ and $z_s - z_u$, which indicate the comfort, handling and suspension deflection performance, respectively, are summarized in Fig. 6. Six typical test points A1, B1, C1, A2, B2 and C2 shown in Fig. 6 are selected with the damping forces displayed in Fig. 7.

In Fig. 6, the performance resulted from PWA and LDPWA $H_\infty$ algorithms will reach the same level when $w_{\max}$ increases to a certain value. Specifically, the RMS values at points C1 and C2 are almost equal. This is because the $w_{\max}$ is much higher than the actual disturbance energy. In other words, controllers designed to handle serve disturbances actually deal with relatively weak disturbances. As a result, in Fig. 7, the damping forces at C1 and C2 are both seriously compressed, which limits the performance of MR dampers. When $w_{\max}$ falls to the values at B1 and B2, the comfort performance under both algorithms is improved. This is because that the performance of MR dampers is released, and the range of damping force at B1 and B2 is significantly expanded compared to that at C1 and C2. Meanwhile, the expanded damping force will inevitably make the suspension "softer", which deteriorates the handling performance and extends the suspension deflection. Comparing the damping forces at B1 and B2, it can be found that the force operating range of LDPWA-$H_\infty$ algorithm is significantly larger than that

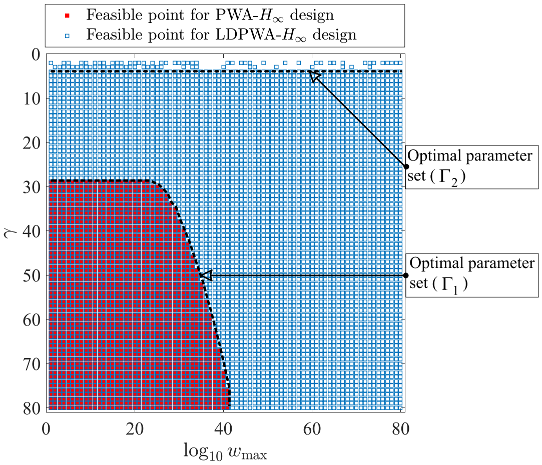

**Fig. 5.** Feasibility of PWA-$H_\infty$ and LDPWA-$H_\infty$ algorithms under different design parameters.

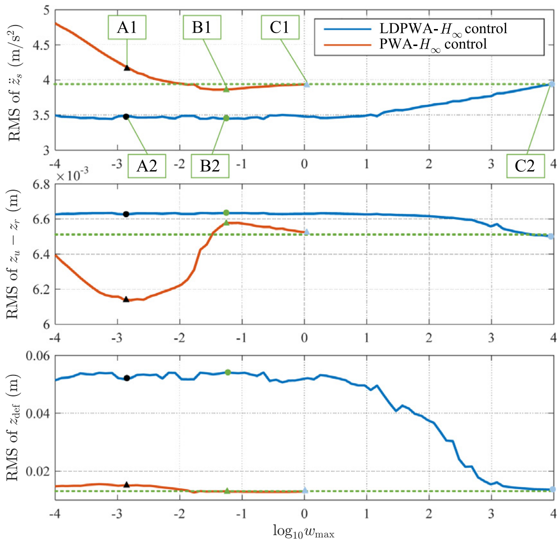

**Fig. 6.** Suspension performance resulted from different values of $w_{\max}$ in set $\Gamma_1$ and $\Gamma_2$.

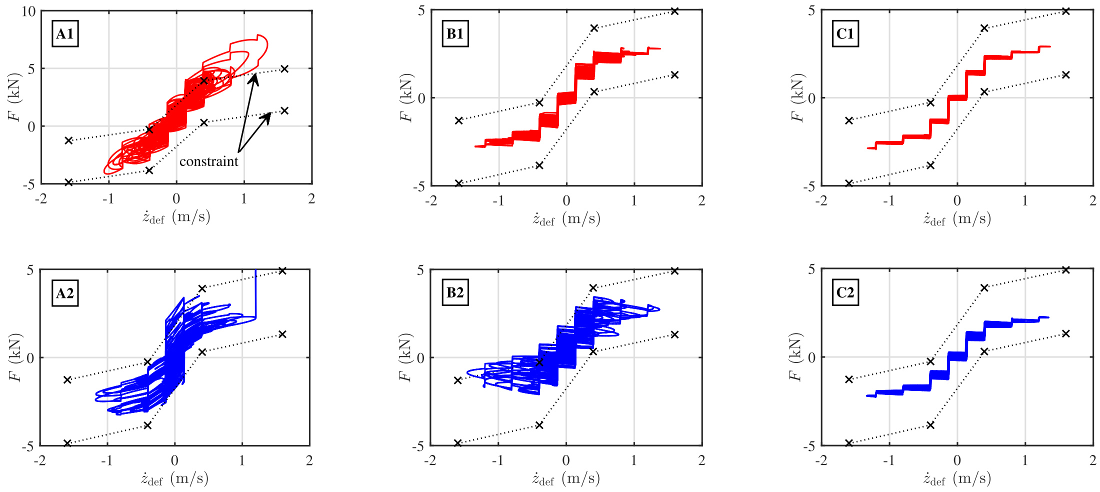

**Fig. 7.** Damping force resulted from different values of parameter $w_{\max}$: PWA-$H_\infty$ algorithm (A1, B1, C1); LDPWA-$H_\infty$ algorithm (A2, B2, C2).

of PWA-$H_\infty$ algorithm. Actually, the output of LDPWA-$H_\infty$ algorithm occupies almost the entire available force region. Therefore, with a slight deterioration in handling performance, LDPWA-$H_\infty$ algorithm achieves significantly better comfort performance than PWA-$H_\infty$ algorithm. Although the suspension deflection at B2 is bigger than that at B1, it is still within acceptable limits. When $w_{\max}$ is lowered to the values at A1 and A2, the damper performance is further released. However, the output of PWA-$H_\infty$ algorithm in Fig. 7 exceeds the constraint (especially the output at post-yield regions), and results in a fairly "stiff" suspension characteristic. Therefore, the comfort performance given by PWA-$H_\infty$ algorithm becomes very poor, and the handling performance is unexpectedly good. Conversely, the output of LDPWA-$H_\infty$ algorithm still satisfies the tortuous constraint and fills the entire reachable region. This is exactly the effect of the piecewise Lyapunov function. In summary, compared to PWA-$H_\infty$ algorithm, the proposed LDPWA-$H_\infty$ algorithm can better utilize damper performance, and can maintain the designed performance over a larger parameter range.

According to above analysis, the principles to choose appropriate design parameters can be derived as that: (1) the nonlinear constraint of the damping force should be fully satisfied; and (2) the ability of MR dampers should be used as much as possible. Following these principles, the parameters of the two $H_\infty$ algorithms in this paper are selected as follows:

- PWA-$H_\infty$: (parameters at point B1) $\gamma = 32, w_{\max} = 0.05$;
- LDPWA-$H_\infty$: (parameters at point A2) $\gamma = 5, w_{\max} = 0.001$.

By designing the controller according to the above parameters and performing closed-loop simulations, the suspension responses shown in Fig. 8 can be obtained. According to the RMS and peak-to-peak (PP) values in Fig. 8(a), we can find that LDPWA-$H_\infty$ algorithm enhances the comfort performance more significantly than PWA-$H_\infty$ algorithm and passive suspensions (In this paper, passive suspensions are represented by MR suspensions driven by constant electric currents, and 0 A and 3 A denote the soft and hard damping properties, respectively.). The same conclusion can also be drawn from the time-domain results shown in Fig. 8(b). In summary, the proposed LDPWA-$H_\infty$ algorithm provides less conservatism than PWA-$H_\infty$ algorithm, and the potential of MR dampers has been further explored.

### 4.3. Analysis of load-adaptive performance

Based on the above selected parameters, this section will analyze the load-adaptive performance of the proposed LDPWA-$H_\infty$ algorithm. To this end, two load conditions are considered here:

- an *underload* condition with $m_s = m_1$;
- an *overload* condition with $m_s = m_2$.

For LDPWA-$H_\infty$ algorithm, we consider two situations for the above conditions:

- (*variable gain*-VG): the time-varying sprung mass is accurately estimated, thus $\hat{m}_s = m_s$;
- (*constant gain*-CG): the sprung mass is estimated incorrectly and the estimated value is a constant nominal value, thus $\hat{m}_s = \bar{m}$.

The performance of passive suspensions will also be analyzed to verify the necessity and effectiveness of load-adaptive properties. To evaluate this property within a concerned frequency range of 0 Hz-25 Hz, the simulations are set to drive the vehicle on a Class C road at a speed of 50 km/h, and the comfort and handling performance will be characterized by the PSD (power spectral density) results of signals $\ddot{z}_s$ and $z_u - z_r$, respectively.

Fig. 9 gives the PSD results of passive suspensions. To facilitate analysis and descriptions, the entire frequency range in Figs. 9 is divided into a low-frequency band (LFB: 0 Hz–2 Hz), a medium-frequency band (MFB: 2 Hz–10 Hz) and a high-frequency band (HFB: 10 Hz–25 Hz). The MFB can also be regarded as the sensitive frequency band of the human body which is generally 4 Hz-8 Hz. Additionally, the resonant frequencies of sprung and unsprung masses are labeled SRF and URF, respectively. By comparing the resonant frequencies of soft and hard suspensions in Fig. 9, it is obviously that increase in load makes SRF shift to a smaller frequency point, while the URF is not influenced. In addition, according to Fig. 9(a), heavier load makes the comfort performance in MFB and HFB better. These phenomena are reasonable since the inertia of the sprung mass increases with load. Accordingly, conclusions can be drawn as that: (1) For underload conditions, it is more necessary to suppress vibrations in the MFB and HFB; (2) For overload condition, the performance within the LFB is more urgent.

Figs. 10 and 11 show the PSD results of LDPWA-$H_\infty$ controlled suspensions and the passive ones, where Fig. 10 is obtained in the underload condition and Fig. 11 displays the overload condition. The forces output by LDPWA-$H_\infty$ controllers are given in Fig. 12.

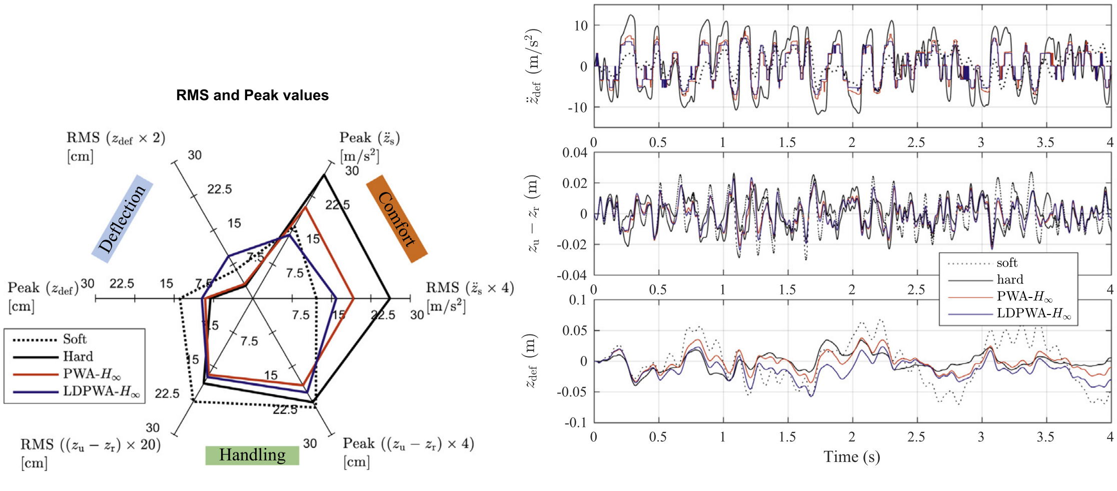

(a) (b)

**Fig. 8.** Performance of PWA and LDPWA $H_\infty$ algorithms under the chosen design parameters: (a) RMS and peak values; (b) time-domain responses.

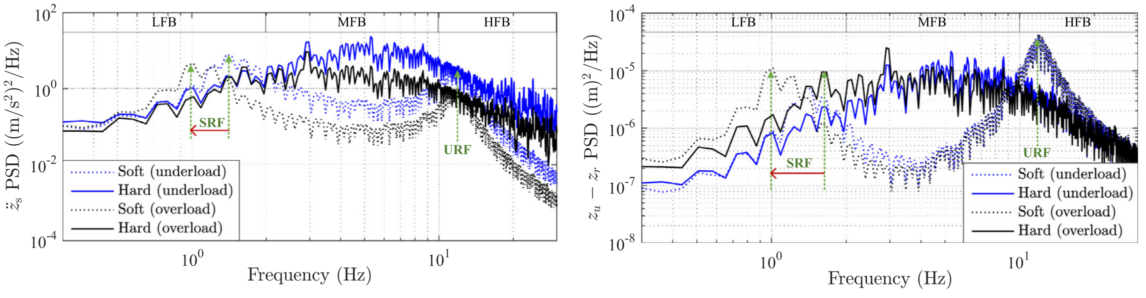

(a) (b)

**Fig. 9.** PSD responses of passive suspensions under different load conditions: (a) comfort performance; (b) handling performance.

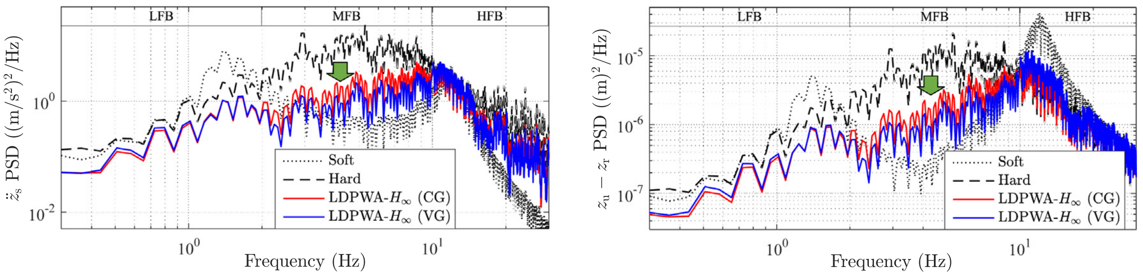

(a) (b)

**Fig. 10.** PSD results of LDPWA-$H_\infty$ controlled semi-active suspensions in underload condition: (a) comfort performance; (b) handling performance.

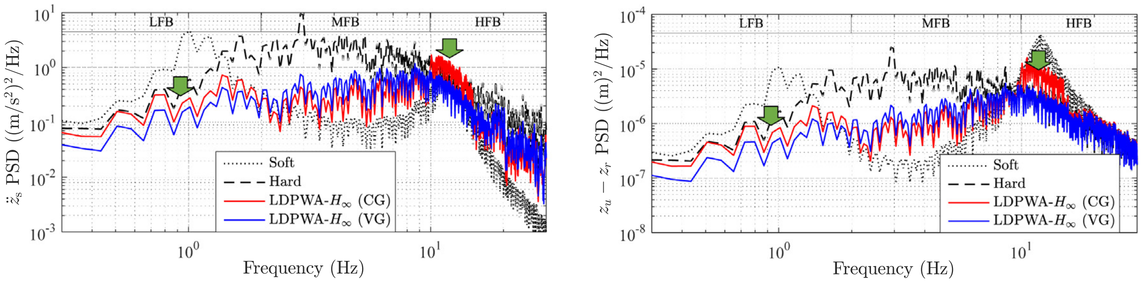

(a) (b)

**Fig. 11.** PSD results of LDPWA-$H_\infty$ controlled semi-active suspensions in overload condition: (a) comfort performance; (b) handling performance.

By comparing the results under the underload condition in Fig. 10, it can be found that the LDPWA-$H_\infty$ algorithm with variable gain has better comfort and handling performance in the MFB than the constant gain algorithm. This phenomenon can be explained by referring to Fig. 9(a), where the variable gain controller gives a softer damping characteristic and the constant gain controller exhibits steeper V/F characteristic. Since the performance within the MFB is more necessary under underload condition, the variable gain controller is preferred. Conversely, for the overload case in Fig. 11, it can be seen that the variable gain controller performs better in LFB and HFB, while the constant gain controller has a slight advantage in MFB. According to Fig. 12(b), this phenomenon can be explained by the fact that the damping characteristic given by the variable gain controller changes to stiff. This is significantly good, not only for vibration attenuation in LFB and HFB, but also for the improvement of cargo capacity. Based on the above analysis, the proposed LDPWA-$H_\infty$ algorithm can adapt to the load variation, and exhibit desired suspension performance.

### *4.4. Comparisons with PWA-$H_\infty$ and SH-ADD algorithms*

In this subsection, the proposed LDPWA-$H_\infty$ controller will be further analyzed by comparing with PWA-$H_\infty$ and SH-ADD controllers. Since the PWA-$H_\infty$ and the SH-ADD algorithms do not have load-adaptive features, only the simulation under

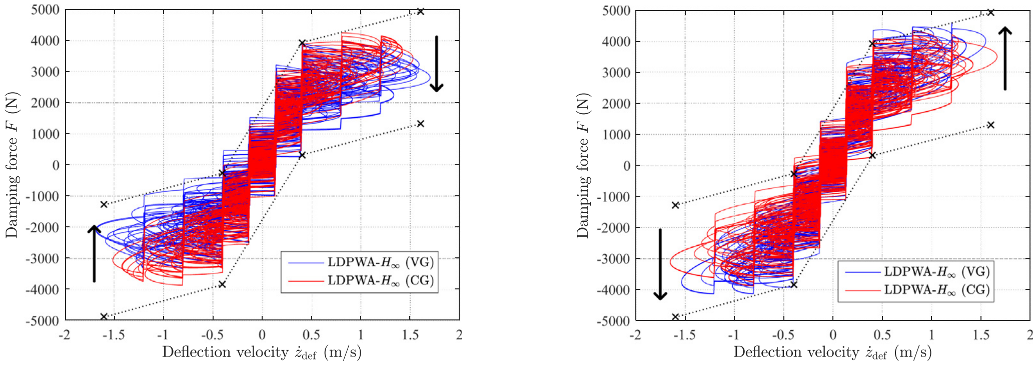

(a)

(b)

**Fig. 12.** Output damping force of LDPWA-$H_\infty$ controllers: (a) underload condition; (b) overload condition.

nominal load will be considered here. Both random and bumpy road profiles will be employed to test the semi-active suspensions.

### 4.4.1. Random road simulations

For random road simulations, vehicles equipped with semi-active suspensions or passive suspensions are designated to travel on Class C roads at a speed of 50 km/h. Fig. 13(a) and (b) show the PSD results for response signals $\ddot{z}_{\mathrm{s}}$ and $z_{\mathrm{u}} - z_{\mathrm{r}}$, respectively. The time-domain responses of signal $\ddot{z}_{\mathrm{s}}$ are given in Fig. 14(a), and (b) gives the corresponding RMS and PP values. Similar results for signal $z_{\mathrm{u}} - z_{\mathrm{r}}$ are displayed in Fig. 15.

Comparing the PSD results of the two $H_\infty$ controllers in Fig. 13, it is obvious that the proposed LDPWA-$H_\infty$ algorithm shows better comfort and handling performance in LFB and MFB. However, in HFB, the performance of the two algorithms

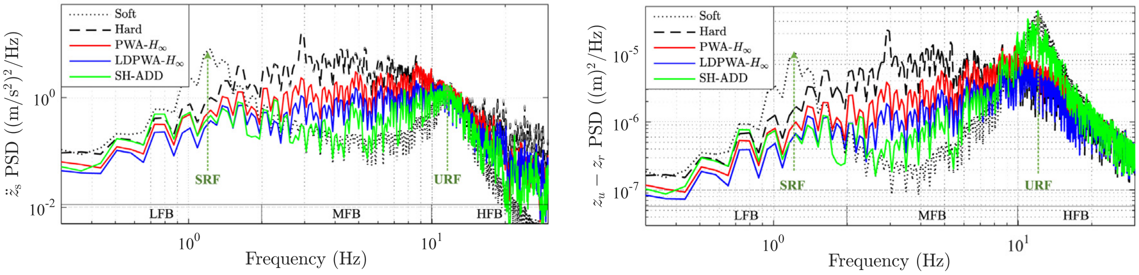

(a)

(b)

**Fig. 13.** PSD results of semi-active suspensions controlled by different algorithms: (a) comfort performance; (b) handling performance.

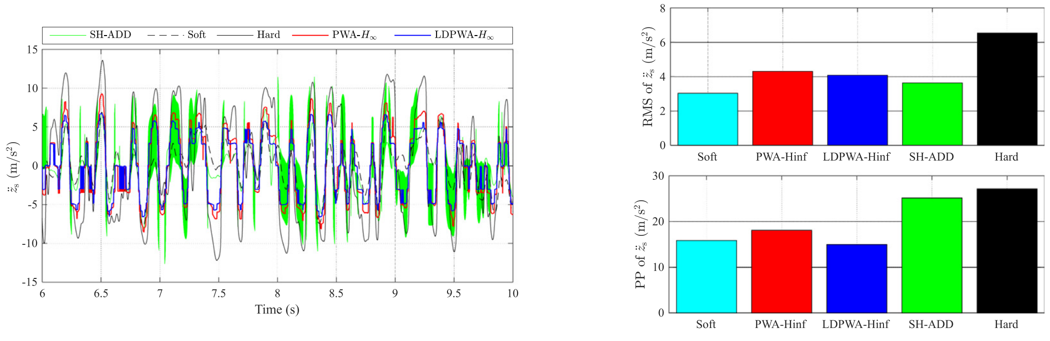

(a)

(b)

**Fig. 14.** Comfort performance of semi-active suspensions controlled by different algorithms: (a) time-domain responses; (b) RMS and PP values.

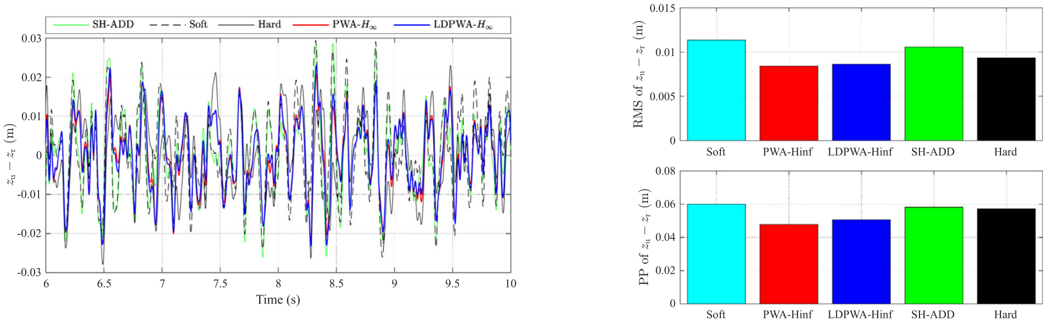

(a) (b)

**Fig. 15.** Handling performance of semi-active suspensions controlled by different algorithms: (a) time-domain responses; (b) RMS and PP values.

is almost the same. Since SRF is smaller than URF, the comfort performance is mainly affected by low-frequency responses, while the handling performance is mainly affected by high-frequency responses. Therefore, we can see that the LDPWA-$H_\infty$ controlled suspension performs better RMS and PP results in Fig. 14, while the indicators of the two $H_\infty$ controllers in Fig. 15 are basically the same. These phenomena are consistent with the results of the previous conservatism analysis.

In Fig. 13(a), the SH-ADD controller exhibits the best comfort performance in MFB and HFB, while the LDPWA-$H_\infty$ controller performs optimally in the LFB. However, in Fig. 13(b), the SH-ADD controlled suspension displays significantly poor performance in the HFB, which is unsatisfactory for the improvement of the handling performance. The RMS and PP results in Fig. 15 also illustrate this shortcoming of the SH-ADD algorithm. Since the SH-ADD algorithm is a comfort-oriented controller, the above results are understandable. Conversely, it can be seen from the results in Figs. 13 and 15 that the proposed LDPWA-$H_\infty$ is capable of achieving good handling performance.

In summary, the proposed LDPWA-$H_\infty$ algorithm shows better comfort performance than the PWA-$H_\infty$ controller, and at the same time, it exhibits better handling performance than the SH-ADD controller. Thus, the multi-objective optimization can be achieved. Additionally, once the human sensibility is considered, the comfort performance in the MFB can be further improved by increasing the weight parameter $\rho_1$, but this will inevitably cause deterioration of the handling performance in the HFB.

It is worth noting that the RMS indicator and the PP indicator of the SH-ADD controlled suspension in Fig. 14(b) is not consistent. Specifically, the RMS value obtained by the SH-ADD controller is obviously better than those of other controllers, which can be interpreted according to the PSD results in 13(a). However, the PP indicator obtained by the SH-ADD controller is very poor, which can also be found from the time-domain responses in Fig. 14(a). This phenomenon will be further analyzed in the following simulations.

### 4.4.2. Bumpy road simulations

To analyze the time-domain responses and the control effect under impact disturbance, the simulation condition that the vehicle travels through an isolated bump is considered. The road profile is simulated by the following expression:

$$z_r(t) = \begin{cases} \frac{A}{2}\left(1-\cos\left(\frac{2\pi Vt}{L}\right)\right), & \text{if } \frac{l}{V} < t < \frac{l+L}{V} \\ 0, & \text{otherwise} \end{cases} \tag{38}$$

where $A$ and $L$ are the height and length of the bump, respectively; $l$ is the length of the flat road ahead of the bump; and $V$ is the vehicle speed. These parameters are chosen as that $V = 36$km/h, $A = 0.3$m, $L = 10$ m, and $l = 10$ m. Fig. 16 shows the time-domain responses and the PP values of signals $\ddot{z}_s$ and $z_u - z_r$. Correspondingly, the control output of corresponding algorithms is given in Fig. 17.

As can be seen from Fig. 16, all three algorithms achieve short settling time when the vehicle has passed through the bump. However, the PP values obtained by each algorithm are different. Specifically, the PP value resulted from the LDPWA-$H_\infty$ controller is the smallest, while the peaks obtained by the SH-ADD controller are extremely poor at 1.3s and 1.7s. In fact, the PP value of the SH-ADD controlled suspension is similar to that of the soft suspension, while the PWA-$H_\infty$ controlled suspension is closer to the hard suspension.

The above results can be explained by analyzing Fig. 17. Firstly, inspired by the switching principle of the SH-ADD algorithm, we divide the damping force in the range of 1s to 2s into four regions. It can be seen that the damping force output by closed-loop algorithms in each region is very close to that of the soft or hard suspension. For example, from 1s to 1.25s, all the three algorithms behave like the hard suspension, and from 1.25s to 1.5s, their damping forces are closer to that of the soft suspension. That is to say, PWA-$H_\infty$ and LDPWA-$H_\infty$ controllers also imply a switching mechanism. Further, it can be found that each switching behavior in Fig. 17 corresponds to a peak in Fig. 16. To analyze the relationship between the peaks and the switching, the damping switching at 1.5s (*hard* to *soft*) is taken as an example in Fig. 17. Then, we can see that, for the

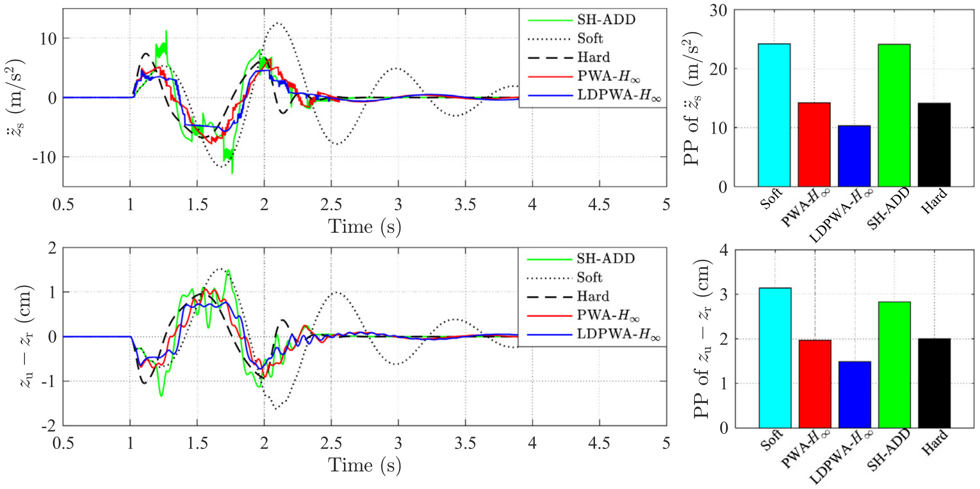

**Fig. 16.** Time-domain responses of different control algorithms under an isolated bump.

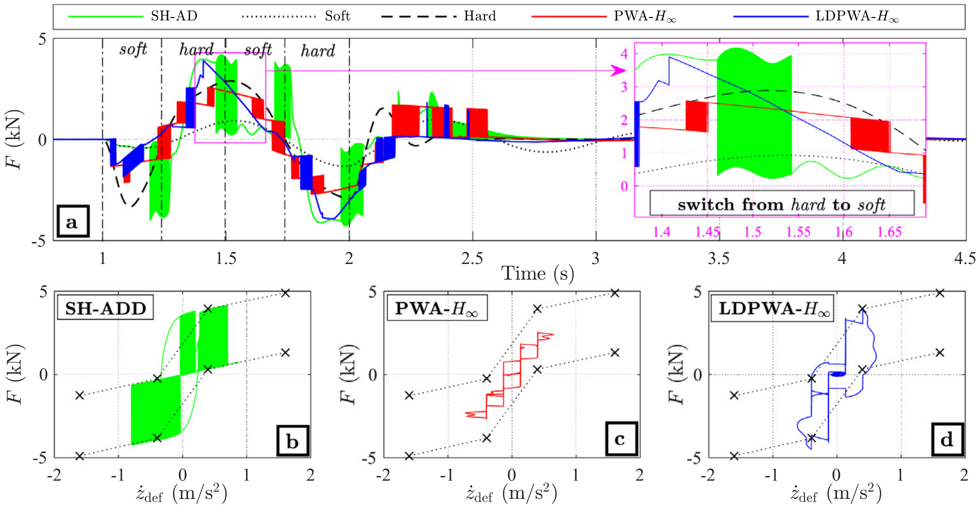

**Fig. 17.** Damping forces of different control algorithms under an isolated bump: a. damping force in time domain; b. V/F property of PWA-$H_\infty$ algorithm; c. V/F property of SH-ADD algorithm; d. V/F property of LDPWA-$H_\infty$ algorithm.

SH-ADD algorithm, this switch happens instantly after a short-time oscillation. However, this oscillation will give rise to a conspicuous peak in Fig. 12. For the PWA-$H_\infty$ algorithm, the switch happens with a terraced reduction in the damping force, which is reasonable since the damper performance is restrained by the GQLF. This terraced switch is too slow, which makes the force trajectory similar to that of the hard suspension in a long-time range. Unlike the two algorithms, the proposed LDPWA-$H_\infty$ algorithm carries out this switch with a slope on the damping force, thus the oscillation will not occur, and the switch will be faster than that of the PWA-$H_\infty$ algorithm. Additionally, the damping oscillation here can also explain the poor PP performance of the SH-ADD algorithm in Fig. 14. Since the damping oscillation happens with a pure high frequency, the suspension performance reflected by PSD and RMS results in Figs. 13 and 14 will not be influenced.

In this subsection, the advantage of taking up more available region of the damping force has been verified again and the superiorities of the proposed LDPWA-$H_\infty$ algorithm have been displayed. However, part of the damping force in Fig. 17 outputted by the LDPWA-$H_\infty$ algorithm has exceeded the constraint boundary. This is because that the energy of this impact disturbance is larger than the design value of $w_{\max}$. A road adaptive controller may achieve better performance, which is out of the scope of this paper.

## 5. Experiment results

An experiment system shown in Fig. 18 which includes a test rig (TR) and a measurement and control system (MCS) will be used to test the proposed algorithm. The TR can simulate the vertical vibration of suspension systems when a vehicle with

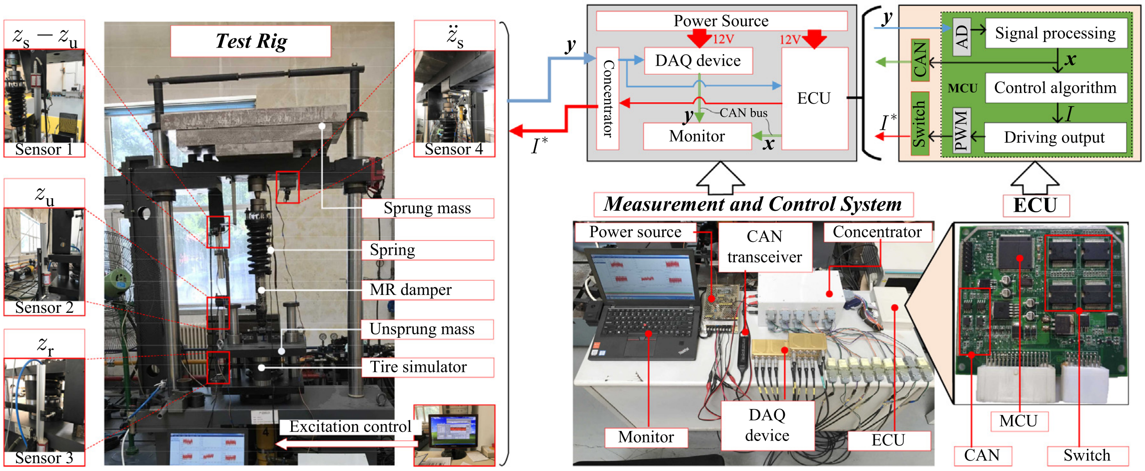

**Fig. 18.** Experiment system for MR semiactive suspensions.

nominal load is running on sinusoidal road profiles (limited by the ability of this test rig, only frequencies under 6 Hz can be tested).Three deflection sensors are assembled in the TR to measure the suspension deflection ($y_1 = z_s - z_u$), the unsprung mass displacement ($y_2 = z_u$), and the road height (simulated by a hydraulic actuator, $y_3 = z_r$). An accelerometer is used to measure the sprung mass acceleration ($y_4 = \ddot{z}_s$). Parameters of this test rig are same with those used in the previous simulations, and the property of the MR damper coincides with the values given in Table 1 (The passive damping $c_s$ is simulated by imposing a small shift to the driving current [26]). Equipments which make up the MCS are shown in Fig. 18, where a concentrator provides the interaction interface between the TR and the MCS, and a data acquisition (DAQ) device from the IPETRONIK company is used to record the signals which are transmitted by a CAN (Controller Area Network) transceiver from the TR and the designed ECU. The power supply of this MCS is a direct current (DC) of 12 V, which can be easily obtained from the vehicle battery. Moreover, the ECU satisfies the application requirements of actual vehicles. Specifically, a 32-bit MCU (micro-controller unit: MPC5643L, 120 MHz) from the NXP semiconductors, which addresses the ISO 26262 safety standard, is employed to run the control algorithms and a power switch from the ST microelectronics is used to drive the MR damper. The power switch is driven by PWM (pulse width modulation) signals with an adjustable duty cycle which corresponds to different electric current values. The signals are obtained from the sensors in analog form. Therefore, AD (Analog to Digital) modules in the MCU will be used. Further, by defining $\mathbf{y} = [z_s - z_u \; z_u \; z_r \; \ddot{z}_s]^T$, the feedback signals of the $H_\infty$ controllers were obtained from the digital signals by using the following filters:

$$x_1 = \frac{1}{\tau s + 1} y_1, \quad x_2 = \frac{1}{\tau s + 1}(y_2 - y_3), \quad x_3 = \frac{s + \xi}{\tau s + 1}(y_1 + y_2), \quad x_4 = \frac{s + \xi}{\tau s + 1} y_2$$

where $\tau = 0.015, \xi = 0.01, 1/(\tau s + 1)$ is a low pass filter for eliminating the high-frequency noise, and $(s + \xi)/(\tau s + 1)$ is a differential filter. For the SH-ADD control purpose, the sprung mass acceleration is also filtered as that $y_4/(\tau s + 1)$. Considering the fast response of MR dampers, the system control period of the ECU is set as 1 ms for all the tested algorithms.

Based on this experiment system, the responses under sinusoidal excitations of different frequencies can be obtained. Further, to give a global view on the concerned frequency range, the experimental results are summarized as the frequency–response (FR) characteristic of the suspension system. According to [44], the FR characteristic of nonlinear systems can be approximated with a *describing function* method. Thus, when a nonlinear system is driving by a sinusoidal excitation of a pure frequency, the approximated FR magnitude under this frequency can be calculated with the variance gain from the disturbance to the system output. For example, the FR magnitude of the sprung mass acceleration (defined as $\widehat{A}_{acc}$) under a frequency $\omega$ can be obtained as that:

$$|\widehat{A}_{acc}(j\omega)| = 20\log_{10}\left(\sqrt{\frac{\int_0^T (\ddot{z}_s(t))^2 dt}{\int_0^T (z_r(t))^2 dt}}\right). \tag{39}$$

Similarly, the FR magnitude of the tire deflection (defined as $\widehat{A}_{ur}$) can be obtained. Based on this method, the FR characteristic of the simulation system in Fig. 18, and the experimental system in Fig. 18 can be both obtained. Specifically, Figs. 19(a) and 19(b) are the simulated FR results from $z_r$ to $\ddot{z}_s$ and $z_u - z_r$, respectively, and Figs. 20(a) and 20(b) are the corresponding experimental results.

In Fig. 19, the LDPWA-$H_\infty$ algorithm shows better comfort and handling performance than the SH-ADD algorithm in LFB. Additionally, the performance of the LDPWA-$H_\infty$ algorithm in MFB is obviously better than that of the PWA-$H_\infty$ algorithm

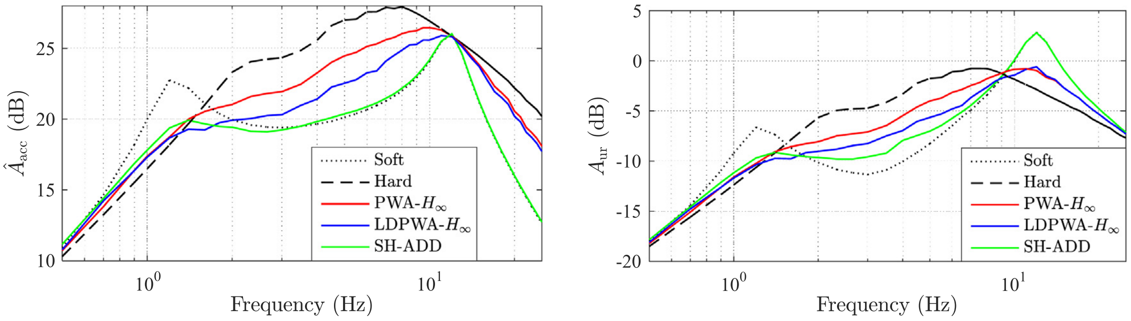

(a) (b)

**Fig. 19.** Approximated frequency responses of the simulation system: (a) $\ddot{z}_s$; (b) $z_u - z_r$.

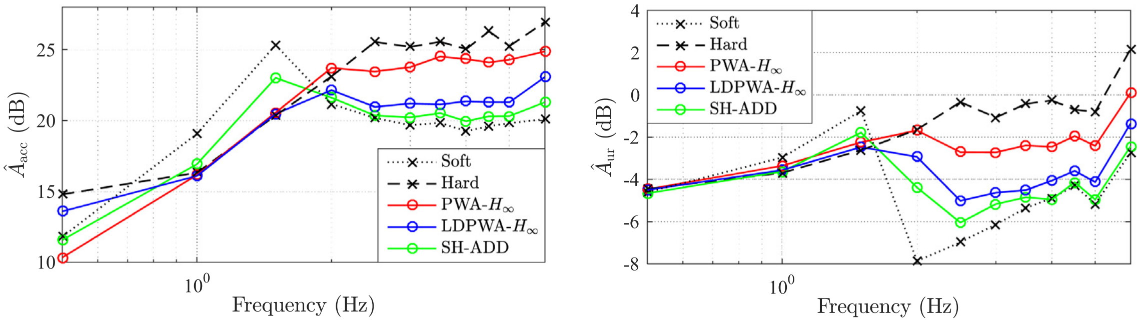

(a) (b)

**Fig. 20.** Approximated frequency responses of the experiment system: (a) $\ddot{z}_s$; (b) $z_u - z_r$.

and can approach the effect of the SH-ADD controlled suspension. These results are consistent with the those obtained through the random road simulations. More importantly, the same conclusion can also be derived from experimental results in Figs. 20. In HFB, Fig. 19(b) shows that the LDPWA-$H_\infty$ and PWA-$H_\infty$ algorithms can both attenuate the vibration of unsprung mass, while the performance of SH-ADD algorithm is unsatisfactory for the enhancement of handling performance. Therefore, a cross-validation has been given for the proposed algorithm under the whole concerned frequency range. Additionally, the experiment results obtained through an actual ECU also confirm the applicability of the proposed LDPWA-$H_\infty$ algorithm for a practical application environment.

## 6. Conclusion

An LDPWA-$H_\infty$ algorithm for MR semi-active suspensions has been given in this paper to deal with the load variation and road disturbance. To guarantee the designed system performance, the nonlinear constraint on the damping force is handled with a piecewise approximation method and a piecewise affine controller. Further, the PDPQLF is used to reduce the system conservatism and to obtain a load-adaptive property for the closed-loop system. Simulation results under random and bumpy road profiles have been studied. Specifically, the proposed algorithm can reveal a stiff damping property for overload conditions and a soft damping property for underload conditions. Further, compared with the GQLF-based PWA-$H_\infty$ algorithm, the proposed algorithm can utilize the available force region of MR dampers much better, which results to better comfort and handling performance. While comparing with the classic SH-ADD algorithm, the proposed algorithm can achieve better handling performance under random road profiles and avoid the oscillation of damping force under bumpy roads. In the end, the superiority of the proposed algorithm under LFB, which results from the full utilization of MR dampers, has been verified by experiments.

## Acknowledgement

This work was supported by China Automobile Industry Innovation and Development Joint Fund [Grant No. U1564213]. The authors would like to thank the FAW-Tokico Corporation for providing the MR damper and the experimental conditions.

## Appendix A

**Lemma 1.** [46]: Let $\lambda(\mathbf{P})$ be a matrix expression that may relate to **P**, or may have nothing to do with **P**. Then, there exists a positive-definite matrix $\mathbf{P} > 0$ such that

$$\begin{bmatrix} -\lambda(\mathbf{P}) & \star \\ \mathbf{PA} & -\mathbf{P} \end{bmatrix} < 0$$

if and only if there exist a positive-definite matrix $\mathbf{P} > 0$ and a matrix **R** such that

$$\begin{bmatrix} -\lambda(\mathbf{P}) & \star \\ \mathbf{R}^{\mathrm{T}}\mathbf{A} & \mathbf{P} - \mathbf{R} - \mathbf{R}^{\mathrm{T}} \end{bmatrix} < 0$$

## References

[1] X. Feng, X. Jing, Human body inspired vibration isolation: beneficial nonlinear stiffness, nonlinear damping and nonlinear inertia, Mech. Syst. Signal Pr. 117 (2019) 786–812, https://doi.org/10.1016/j.ymssp.2018.08.040.

[2] M.V. de Wal, P. Philips, B. de Jager, Actuator and sensor selection for an active vehicle suspension aimed at robust performance, Int. J. Control 70 (5) (1998) 703–720, https://doi.org/10.1080/002071798222091.

[3] D. Hrovat, Survey of advanced suspension developments and related optimal control applications, Automatica 33 (10) (1997) 1781–1817, https://doi.org/10.1016/S0005-1098(97)00101-5.

[4] H. Chen, K. Guo, Constrained $H_\infty$ control of active suspensions: an LMI approach, IEEE T. Contr. Syst. T. 13 (3) (2005) 412–421, https://doi.org/10.1109/TCST.2004.841661.

[5] R. Sharp, D. Crolla, Road vehicle suspension system design - a review, Vehicle Syst. Dyn. 16 (3) (1987) 167–192, https://doi.org/10.1080/00423118708968877.

[6] J. Na, Y. Huang, X. Wu, G. Gao, G. Herrmann, J. Jiang, Active adaptive estimation and control for vehicle suspensions with prescribed performance, IEEE T. Contr. Syst. T. PP (99) (2017) 1–15, https://doi.org/10.1109/TCST.2017.2746060.

[7] G. Koch, T. Kloiber, Driving state adaptive control of an active vehicle suspension system, IEEE T. Contr. Syst. T. 22 (1) (2014) 44–57, https://doi.org/10.1109/TCST.2013.2240455.

[8] S. Yan, W. Sun, Self-powered suspension criterion and energy regeneration implementation scheme of motor-driven active suspension, Mech. Syst. Signal Pr. 94 (2017) 297–311, https://doi.org/10.1016/j.ymssp.2017.03.006.

[9] S. Molina, Adaptive load dependent suspension system (03 1998). https://www.lens.org/lens/patent/107-161-259-020-391.

[10] L. Lemmens, J. Schel, Booster with spring to adapt air spring pressure for load dependent shock absorber (08 2006). https://www.lens.org/lens/patent/083-358-596-552-84X.

[11] H. Gao, J. Lam, C. Wang, Multi-objective control of vehicle active suspension systems via load-dependent controllers, J. Sound Vib. 290 (3–5) (2006) 654–675, https://doi.org/10.1016/j.jsv.2005.04.007.

[12] H. Du, N. Zhang, J. Lam, Parameter-dependent input-delayed control of uncertain vehicle suspensions, J. Sound Vib. 317 (3–5) (2008) 537–556, https://doi.org/10.1016/j.jsv.2008.03.066.

[13] I. Maciejewski, S. Glowinski, T. Krzyzynski, Active control of a seat suspension with the system adaptation to varying load mass, Mechatronics 24 (8) (2014) 1242–1253, https://doi.org/10.1016/j.mechatronics.2014.10.008.

[14] X. Ma, P. Wong, J. Zhao, Practical multi-objective control for automotive semi-active suspension system with nonlinear hydraulic adjustable damper, Mech. Syst. Signal Pr. 117 (2019) 667–688, https://doi.org/10.1016/j.ymssp.2018.08.022.

[15] H. Chiang, Y. Chen, K. Hsu, Optimized sensorless antivibration control for semiactive suspensions with cosimulation analysis, IEEE-ASME T. Mech. 20 (4) (2015) 1898–1911, https://doi.org/10.1109/TMECH.2014.2358583.

[16] S. Nguyen, S. Choi, Q. Nguyen, A new fuzzy-disturbance observer-enhanced sliding controller for vibration control of a train-car suspension with magneto-rheological dampers, Mech. Syst. Signal Pr. 105 (2018) 447–466, https://doi.org/10.1016/j.ymssp.2017.12.019.

[17] J. Jason, K. Robert, Load dependent damper for a vehicle suspension system (03 2015). https://www.lens.org/lens/patent/077-905-447-573-80X.

[18] X. Nguyen, T. Komatsuzaki, Y. Iwata, H. Asanuma, Modeling and semi-active fuzzy control of magnetorheological elastomer-based isolator for seismic response reduction, Mech. Syst. Signal Pr. 101 (2017) 449–466, https://doi.org/10.1016/j.ymssp.2017.08.040.

[19] M. Zapateiro, F. Pozo, H. Karimi, N. Luo, Semiactive control methodologies for suspension control with magnetorheological dampers, IEEE-ASME T. Mech. 17 (2) (2012) 370–380, https://doi.org/10.1109/TMECH.2011.2107331.

[20] J. Berasategui, M. Elejabarrieta, M. Bou-Ali, Characterization analysis of a MR damper, Smart Mater. Struct. 23 (4) (2014) , https://doi.org/10.1088/0964-1726/23/4/045025 045025.

[21] G. Iglesias, S. Ahualli, J. Otero, L. Ruiz-Moron, J. Duran, Theoretical and experimental evaluation of the flow behavior of a magnetorheological damper using an extremely bimodal magnetic fluid, Smart Mater. Struct. 23 (8) (2014) , https://doi.org/10.1088/0964-1726/23/8/085028 085028.

[22] X. Bai, F. Cai, P. Chen, Resistor-capacitor (RC) operator-based hysteresis model for magnetorheological (MR) dampers, Mech. Syst. Signal Pr. 117 (2019) 157–169, https://doi.org/10.1016/j.ymssp.2018.07.050.

[23] J. Esmaeili, A. Akbari, H. Karimi, Load-dependent LPV/H_2 output-feedback control of semi-active suspension systems equipped with MR damper, Int. J. Vehicle Des. 68 (1–3) (2015) 119–140, https://doi.org/10.1504/IJVD.2015.071077.

[24] N. Giorgetti, A. Bemporad, H. Tsengz, D. Hrovat, Hybrid model predictive control application towards optimal semi-active suspension, Int. J. Control 79 (5) (2006) 521–533, https://doi.org/10.1080/00207170600593901.

[25] C. Poussot-Vassal, C. Spelta, O. Sename, S. Savaresi, L. Dugard, Survey and performance evaluation on some automotive semi-active suspension control methods: a comparative study on a single-corner model, Annu. Rev. Control 36 (1) (2012) 148–160, https://doi.org/10.1016/j.arcontrol.2012.03.011.

[26] J. Wu, Z. Liu, W. Chen, Design of a piecewise affine $H_{infty}$ controller for MR semiactive suspensions with nonlinear constraints, IEEE T. Contr. Syst. T. (2018) 1–10, https://doi.org/10.1109/TCST.2018.2832127.

[27] M. Canale, M. Milanese, C. Novara, Semi-active suspension control using "fast model-predictive techniques, IEEE T. Contr. Syst. T. 14 (6) (2006) 1034–1046, https://doi.org/10.1109/TCST.2006.880196.

[28] L. Cseko, M. Kvasnica, B. Lantos, Explicit MPC-based RBF neural network controller design with discrete-time actual kalman filter for semiactive suspension, IEEE T. Contr. Syst. T. 23 (5) (2015) 1736–1753, https://doi.org/10.1109/TCST.2014.2382571.

[29] H. Du, K. Sze, J. Lam, Semi-active $H_\infty$ control of vehicle suspension with magneto-rheological dampers, J. Sound Vib. 283 (3–5) (2005) 981–996, https://doi.org/10.1016/j.jsv.2004.05.030.

[30] O. Sename, A. Do, C. Poussot-Vassal, L. Dugard, Some LPV approaches for semi-active suspension control, in: Proc. of ACC, 2012, pp. 1567–1572.

[31] A. Vahidi, A. Stefanopoulou, H. Peng, Recursive least squares with forgetting for online estimation of vehicle mass and road grade: theory and experiments, Vehicle Syst. Dyn. 43 (1) (2005) 31–55, https://doi.org/10.1080/00423110412331290446.

[32] M. Mahyuddin, J. Na, G. Herrmann, X. Ren, P. Barber, Adaptive observer-based parameter estimation with application to road gradient and vehicle mass estimation, IEEE T. Ind. Electron. 61 (6) (2014) 2851–2863, https://doi.org/10.1109/TIE.2013.2276020.

[33] S. Sharma, A. Kumar, Ride performance of a high speed rail vehicle using controlled semi active suspension system, Smart Mater. Struct. 26 (5) (2017) , https://doi.org/10.1088/1361-665X/aa68f7 055026.

[34] S. Sharma, A. Kumar, Disturbance rejection and force-tracking controller of nonlinear lateral vibrations in passenger rail vehicle using magnetorheological fluid damper, J. Intel. Mat. Syst. Str. 29 (2) (2018) 279–297, https://doi.org/10.1177/1045389X17721051.

[35] S. Nguyen, W. Kim, J. Park, S. Choi, A new fuzzy sliding mode controller for vibration control systems using integrated-structure smart dampers, Smart Mater. Struct. 26 (4) (2017) , https://doi.org/10.1088/1361-665X/aa52fd 045038.

[36] M. Johansson, Piecewise linear control systems, Springer, Berlin, 2003, Ch. Lyapunov stability, pp. 41–84.

[37] R. Stanway, J. Sproston, A. Elwahed, Applications of electro-rheological fluids in vibration control: a survey, Smart Mater. Struct. 5 (4) (1996) 464–482, https://doi.org/10.1088/0964-1726/5/4/011.

[38] S. Hong, N. Wereley, Y. Choi, S. Choi, Analytical and experimental validation of a nondimensional bingham model for mixed-mode magneto rheological dampers, J. Sound Vib. 312 (3) (2008) 399–417, https://doi.org/10.1016/j.jsv.2007.07.087.

[39] B. Spencer, S. Dyke, M. Sain, J. Carlson, Phenomenological model for magnetorheological dampers, J. Eng. Mech.-ASCE 123 (3) (1997) 230–238. doi:10.1061/(ASCE)0733-9399(1997) 123:3(230).

[40] S. Nguyen, H. Ho, T. Nguyen, N. Truong, T. Seo, Novel fuzzy sliding controller for mrd suspensions subjected to uncertainty and disturbance, Eng. Appl. Artif. Intel. 61 (2017) 65–76, https://doi.org/10.1016/j.engappai.2017.03.002.

[41] S. Guo, S. Yang, C. Pan, Dynamic modeling of magnetorheological damper behaviors, J. Intel. Mat. Syst. Str. 17 (1) (2006) 3–14, https://doi.org/10.1177/1045389X06055860.

[42] J. Lozoya-Santos, R. Morales-Menendez, R. Ramirez-Mendoza, J. Tudon-Martinez, O. Sename, L. Dugard, Magnetorheological damper-an experimental study, J. Intel. Mat. Syst. Str. 23 (11) (2012) 1213–1232, https://doi.org/10.1177/1045389X12445035.

[43] T. Schmelzer, R. Hauser, E. Andersen, J. Dahl, Regression techniques for portfolio optimisation using mosek, arXiv preprint arXiv:1310.3397.

[44] S. Savaresi, C. Spelta, Mixed sky-hook and ADD: approaching the filtering limits of a semi-active suspension, J. Intel. Mat. Syst. Str. 129 (4) (2007) 382–392, https://doi.org/10.1115/1.2745846.

[45] C. Dharankar, M. Hada, S. Chandel, Numerical generation of road profile through spectral description for simulation of vehicle suspension, J. Braz. Soc. Mech. Sci. 39 (6) (2017) 1957–1967, https://doi.org/10.1007/s40430-016-0615-6.

[46] Y. Jia, Alternative proofs for improved LMI representations for the analysis and the design of continuous-time systems with polytopic type uncertainty: a predictive approach, IEEE T. Automat. Contr. 48 (8) (2003) 1413–1416, https://doi.org/10.1109/TAC.2003.815033.